DOE/ET-53088-197 IFSR #197

EXPLOSIVE COALESCENCE OF MAGNETIC ISLANDS AND EXPLOSIVE PARTICLE ACCELERATION

T. Tajima
Institute for Fusion Studies
The University of Texas at Austin
Austin, Texas 78712

J.-I.Sakai
Department of Applied Mathematics and Physics
Faculty of Engineering
Toyama University
Toyama, 930 JAPAN

July 1985

EXPLOSIVE COALESCENCE OF MAGNETIC ISLANDS AND PARTICLE ACCELERATION

T. Tajima

Institute for Fusion Studies and Department of Physics

The University of Texas at Austin

Austin, Texas 78712-1081

and

J.-I. Sakai

Department of Applied Mathematics and Physics

Faculty of Engineering

Toyama University

Toyama, 930 Japan

Abstract

An explosive reconnection process associated with the nonlinear evolution of the coalescence instability is found through studies of the electromagnetic particle simulation and the magnetohydrodynamic particle simulation. The explosive coalescense is a process of magnetic collapse, in which we find the magnetic and electrostatic field energies and temperatures (ion temperature in the coalescing direction, in particular) explode toward the explosion time t_0 as $(t_0 - t)^{-8/3}$, $(t_0 - t)^{-4}$, and $(t_0 - t)^{-8/3}$, respectively. Single-peak, double-peak, and triple-peak structures of magnetic energy, temperature, and electrostatic energy, respectively, are observed on the simulation as overshoot amplitude oscillations and these features are theoretically explained. The heuristic model of Brunel, Tajima and Dawson is extended to this explosive coalescence in order to extract the basic process. Since the explosive coalescence exhibits self-similarity, a temporal universality, we theoretically search for a self-similar solution to the two-fluid plasma equations. Our theory produces the indices of explosion in agreement with our simulation results. The governing equation for the scale factor takes a form of the orbital equation in a Sagdeev potential, in which the potential energy assumes a form of the gravitational potential and the centrifu-

gal energy. For the coalescence to become explosive, the "total energy" has to be close to zero and the plasma β value to be small. Such a situation is realized for the peaked current distributions. The explosion time is given as $\sqrt{2}a_0^{3/2}t_A/3$, where a_0 is the scale factor at t=0 and t_A the Alfvén time. Explosive acceleration of particles binormal to the magnetic field B_y and electrostatic field E_x becomes possible during the magnetic collapse and yields the maximum momentum $p_z^{\max} \simeq m_0 c(E_x/B_y)/[1-(E_x/B_y)]^{1/2}$, as E_x^2 diverges faster than B_y^2.

I. Introduction

A crucial process in the study of magnetohydrodynamic (MHD) activities of tokamak plasmas,[1] reverse-field pinch plasmas,[2] and field reverse configuration plasmas[3] is that of magnetic field-line reconnection and tearing. Examples of phenomena that involve this process include the major and internal disruption of tokamak confinement,[1,4,5] the externally sustained reverse field configuration[2] and its deterioration, and the rapid decay of a plasma after the tilting instability.[6] It is also essential to cosmic plasmas such as in solar flares[7,8,9] and in the magnetosphere,[10,11] in which the magnetic energy is converted into kinetic energy when there occur intense magnetic disturbances.

In these problems the reconnection of field-lines is believed to take place due to finite resistivity $\eta = c^2/4\pi\sigma$ (be it small). The relative magnitude of the time scale for magnetic field-line reconnection may be characterized by the magnetic Reynolds number (or the Lunquist number) $R_m = \tau_r/\tau_A$ or a smallness parameter, the inverse of Reynolds number, $\epsilon = R_m^{-1}$. Thus the time scale of reconnection due to the mechanism of the tearing instability is characterized by $\epsilon^{-3/5}$. Sweet and Parker[7] obtained a steady-state solution which has a narrow x-point angle; the time scale τ_{SP} of reconnection is characterized[7,12] by $\tau_{SP}^{-1} = \eta^{1/2}(n_i/n_e)^{1/2}(v_A/L)^{1/2}1/x_0 \propto \eta^{1/2}$, where $2L$ is the length of the impinged plasma, n_i and n_e are the densities inside and outside of the singular layer.[12] Petschek[8] similarly obtained a steady-state solution which has a large x-point angle; the reconnection time scale τ_P is independent of resistivity, $\tau_P^{-1} \propto \eta^0$. The time scale of reconnection due to the mechanism of the Sweet-Parker process is characterized by $\epsilon^{-1/2}$, while that of Petschek is by ϵ^0. Here we use the words, driven reconnection, in a broad context in which reconnection of magnetic field-lines is incurred so forcibly from external forces that the reconnection process is essentially nonlinear, exhibiting no reminiscent linear instability growth.

In order to rapidly convert magnetic energy into kinetic by a substantial amount, it seems necessary that the bulk of magnetic energy has to participate in the conversion process: the resistive heating at the x-point alone is too meager. This is because the available magnetic energy at the x-point is small by itself. On the other hand, the ideal MHD instabilities such as the kink instability and the coalescence instability are the processes

that involve the bulk current redistribution in a matter of the Alfvén time scale.

Nonlinear processes of reconnection either driven by external boundary conditions[12,13,14] or triggered as a secondary process[15] by the primary instability have been investigated. According to Refs. 12 and 14 for the problem of externally driven reconnection the rate of reconnection experiences more than one phase with a sufficiently strong drive and a compressible plasma: the first Sweet-Parker phase were the reconnected flux $\psi \cong \eta^{1/2}t$ and later (after τ_{SP}) the second phase $\psi \cong \eta^{1/2}t^{\alpha}$, where α is determined by the density compression.

In the present paper we are interested in the latter problem, i.e., the nonlinear driven reconnection triggered as a secondary process by the primary instability. In particular we pick the coalescence instability[16,17] as the primary instability to investigate its nonlinear consequences. We do so because (i) although it is an ideal MHD instability in the linear sense, it would not nonlinearly evolve if there were no resistive (non-ideal MHD) effect; (ii) it can involve a large amount of conversion of magnetic to kinetic energies in a short time; (iii) it is essentially a two-dimensional instability, thus more amenable to thorough analysis of the fundamental processes of the instability. It is interesting to observe that with this two-dimensionality restriction we still find an explosive process as we shall see. Generally, it is believed that introduction of an additional dimension (this case, a third dimension) to the problem allows breaking of symmetry that has been kept before the introduction, leading to more or easier paths to relax the system to the "lowest energy state". Therefore, we should be "guaranteed" to have an explosive process in three dimensions through the nonlinear coalescence instability since it was "already" explosive in two dimensions. In Ref. 15 the reconnection was driven by the coalescence instability, the primary instability. The coalescence instability starts from the Fadeev equilibrium,[18] which is characterized by the current localization parameter ϵ_c: The equilibrium toroidal current (in the z-direction) is given as $J_z = B_{ox}k(1-\epsilon_c^2)(\cosh ky + \epsilon_c \cos kx)^{-2}$. The parameter ϵ_c varies from 0 to 1 with small ϵ_c corresponding to a weak localization and ϵ_c close to unity corresponding to a peaked localization; in the limit of $\epsilon_c \rightarrow 1$ the current distribution becomes delta function-like. According to Ref. 15 the rate of reconnection was that of Sweet-Parker for small ϵ_c, while the reconnection rate experiences two phases for

larger ϵ_c (but smaller than 0.8). This emergence of two phases is similar to the case of the driven reconnection.[14] The intensity of coalescence and the rate of subsequent reconnection are controlled by just one parameter, the current localization (ϵ_c). In this problem there is no ambiguity as to the nature of the driver in contrast to the reconnection driven by external boundary conditions. For the case with ϵ_c=0.7, the second phase showed the reconnected flux ψ increasing as t^α with $1 < \alpha \lesssim 2$. This indicates that the more the current localizes, the faster the reconnection becomes.

This leads to a question: Can the reconnected flux ψ increase explosively as $(t_0 - t)^{-\alpha}(\alpha > 0)$ triggered by the coalescence instability? As we shall see in the next section, yes it can, when ϵ_c is increased further to a larger value. In the present section, however, let us show computational results obtained by our electromagnetic particle simulation based on the same parameters as reported in Ref. 19 and on a set-up similar to Ref. 20.

Figure 1 displays the time history of various field and particle quantities observed in our simulation in which after the initial transient (up to t=$4\Omega_i^{-1}$ in the code unit to be explained in the following section) the phase of coalescence of two magnetic islands commences. It is seen in Figs. 1(a)-(c) that around t=27 the magnetic and electrostatic field energies shoot up explosively as well as the ion temperature in the direction of coalescence (the x-direction). The unit of computational time is omitted hereafter whenever it is unambiguous. It is also seen in Figs. 1(a)-(c) that (i) after the explosive increase of the field energies and temperature this overshooting results in synchronous amplitude oscillations of all these quantities with the period being approximately the compressional Alfvén period; and (ii) superimposed on these overall amplitude oscillations is a distinct double-peak structure in the electrostatic field energy and the ion temperature. Although we are interested in analyzing the entire episode of the run including the initial phase and the post-explosive phase, we focus particularly on the explosive phase of the coalescence. We replot Figs. 1(a)-(c) into Figs. 1(d)-(f) to find the way in which these quantities increase toward the catastrophic point. We find from Figs. 1(d)-(f) that (i) the magnetic energy explodes as $(t_0 - t)^{-8/3}$; (ii) the electrostatic energy explodes as $(t_0 - t)^{-4}$; and (iii) the ion temperature in the coalescing direction explodes as $(t_0 - t)^{-8/3}$ until saturation due to overshooting sets in, where t_0 is the explosion time measured here to be $t_0 \sim 27(\Omega_i^{-1})$ in

this run. See Table I.

This discovery of the existence of an explosive process (or instability) and its indices of explosion (the exponent to the time) is important because it tells us that the explosive magnetic process (we may call this the magnetic collapse) can take place in two dimensions and also it prompts our analysis. It is learned that driven reconnection (in the present case it is driven by the coalescence instability) can be explosive under the appropriate conditions. This also underlines a point that the magnetic interaction (the current-current interaction in the manner of Biot-Savart's law) can be inherently attractive and thus explosive (if currents are in the same sense).

As we shall see, it is possible to explain many of these overall as well as detailed aspects of the explosive process. In particular our theory can predict many of these indices of explosion. In addition we observe that as the coalescence process approaches the explosion time $t=t_0$, each quantity tends to saturate, but with a different timing and fashion. During the overshooting and its subsequent recovery period (that of amplitude oscillations) each quantity exhibits a different pattern. These features will be noted and discussed along with our theoretical explanations for these effects.

Our investigation of the coalescence of magnetic islands is through extensive numerical simulations of both MHD and kinetic types. We analyze these results, and then construct a heuristic model of the explosive coalescence and later a more complete theory of this process. The theory that accounts for the explosive coalescence process is then extended to explain the explosive acceleration of particles during this process.

Section II presents a numerical study of the explosive coalescence through the particle simulation as well as the MHD particle simulation. This section goes on to discuss the fundamental physical process underlining the explosive coalescense by presenting the heuristic model that is a generalization of the Brunel-Tajima-Dawson model.[12,14] In Sec. III we polish the generalized Brunel-Tajima-Dawson model for the explosive process and construct a more complete theory. This theory predicts many indices of explosion under various different conditions. The theory is put to comparison with the above simulation observations with reasonable agreement. We expand our theory in Sec. IV to explain the heating and acceleration associated with the explosive coalescence. Again the

comparison of the theory with simulation is compelling. The final section discusses many possible applications of the present discoveries and theory to diverse fields of physics. It also summarizes and gives conclusions.

II. Coalescence of Magnetic Islands

A. Simulation Results

The nonlinear evolution of explosive coalescence of magnetic islands is studied by computer simulation. We combine and compare both an MHD model and a kinetic model of simulation. The results from these two different models are consistent in basic points, but are complementary in many detailed aspects. The results are then analyzed in light of a heuristic model presented later in this section which contains some essential ingredients of the physical process of explosive coalescence.

The kinetic simulation model we adopt here is the electromagnetic particle code[21,22] with $2\frac{1}{2}$ dimensions. The configuration of the plasma and magnetic fields is that of Refs. 19 and 20. The plasma density is initially uniform in the x- and y-directions and the z-direction is the ignorable direction. Fields are solved with periodic boundary conditions in the x- and y-directions. The sheared magnetic fields are generated by the externally imposed sheet currents J_z at y=0 and L_y, where L_y is the length of the periodic box in the y-direction. The sheet currents are turned with a ramp function profile in time. The excess of the plasma return current or lack of it for the uniform component (the wavenumber k=0) is compensated by the displacement current term alone, since the term $\nabla \times B$ vanishes for k=0.[20] There are narrow slits in x where J_z=0, which fix positions of magnetic islands. As discussed in Ref. 20, the other islands are induced in between the islands that are fixed as mentioned in the above. These islands later coalesce. The process of island generation from this configuration was discussed in Refs. 12 and 20. The later process of coalescence of generated islands is our main concern in the present article. A uniform external (toroidal) magnetic field B_z is applied with various chosen strengths. Typical parameters we employ in this code are: the numbers of grid points in the x-and y-directions are L_x/Δ=128 and L_y/Δ=32, the number of electrons (and that of ions) 16384, the speed of light c=$4\omega_{pe}\Delta$, the thermal velocities of electrons in the x-, y-, and

z-directions $v_e = 1\omega_{pe}\Delta$, the electron-to-ion mass ratio m_e/m_i=1/10, the electron-to-ion temperature ratio T_e/T_i=2.0, the (poloidal) sheared magnetic field B_x at y=0 and L_y is such that eB_x/m_ec=0.77ω_{pe}, and the size of particles a=1Δ, where Δ is the unit grid length and ω_{pe} is the electron plasma frequency for the uniform plasma at the initial time. The toroidal field B_z is varied with $eB_z/mc\omega_{pe}$ ranging from 0 to 0.2, 1, and 2.

In these parameters the poloidal Larmor radius at the external current sheets for electrons and ions are ρ_{pe}=1.2λ_{De} and ρ_{pi}=5.3λ_{De}, the poloidal cyclotron frequencies for electrons and ions Ω_e=0.77ω_{pe} and Ω_i=0.077ω_{pe}, and the poloidal Alfvén velocity v_{Ap}=1.22v_e and the poloidal Alfvén transit time measured in terms of the poloidal Alfvén velocity at the sheet with the initial plasma density is $\tau_{Ay} = L_y/v_{Ap} = 26\omega_{pe}^{-1}$ and $\tau_{Ax} = L_x/v_{Ap} = 105\omega_{pe}^{-1}$. These numbers change accordingly when there is an imposed toroidal magnetic field B_z. Because of the nature of the particle code and electromagnetic interactions retained, the temporal and spatial scales of simulation are compressed by using an unrealistically large electron-to-ion mass ratio and small grid. However, it is noted that the main time scales we are interested in are that of the Alfvén time and the electron time scales are sufficiently isolated from this. The chief purpose of this simulation is not to reproduce laboratory plasma behavior but to extract some fundamental underlying processes and try to understand them. In fact, as we shall see, many of the basic characteristics of the simulation findings are reasonably explained by theoretical analysis. Although the fundamental physics emerges in the kinetic simulation, many parameters are strained in this model such as an unrealistically large mass ratio 1/10. On the other hand, the MHD model dispenses many of these processes and thus it is unnecessary to strain many parameters

The MHD simulation model we use is the MHD particle code[23] with $2\frac{1}{2}$ dimensions. The configuration of the plasma and magnetic fields is that of Refs. 15 and 19 based on the initial conditions of Fadeev et al.'s equilibrium.[18] The MHD particle code is robust in applications to problems even with strong turbulence, flows, convections, and density depression. This is helpful because the present problem involves fast (explosive) reconnection, strong density depression and compression, and strong flows. The magnetic induction equation is advanced by the Lax-Wendroff method.[23] The plasma is originally

uniform in density and temperature contained by metallic (conducting) walls at y=0 and L_y. Here typical parameters are: L_x/Δ=128 and L_y/Δ=64, the number of fluid particles 32768, the poloidal magnetic fields B_x at y=0 and L_y are such that the (poloidal) Alfvén velocity v_{Ap}=3.5c_s, the adiabatic constant γ=2, and the size of particles a=1.0Δ, where c_s is the sound speed and Δ is the unit grid length. The current localization parameter ϵ_c is varied from the value ϵ_c=0.3 to 0.85 where ϵ_c appears in the equilibrium current profile as J_z=$B_{ox}k(1-\epsilon_c^2)(\cosh ky+\epsilon_c\cos kx)^{-2}$. The Alfvén transit times across the y-direction and the x-direction are τ_{Ay}=18.3Δ/c_s and τ_{Ax}=36.5Δ/c_s, respectively. The typical magnetic Reynolds number is $R_m \cong 10^4$ with $\eta = 0.036\Delta c_s$.As is well known, the ideal MHD dynamics does not contain any characteristic length, except for the system's overall length; in the present case it is either L_y or the island width. For example, the collisionless skin depth c/ω_{pe} and the Debye length vanish. Therefore, in contrast with the kinetic model discussed earlier, the spatial scales are not compressed. Similarly, the relevant time scales are the Alfvén time and the much larger resistive time. On the other hand, the MHD model largely lacks the kinetic effects such as the Landau and cyclotron dampings, particle acceleration, finite Larmor radius effects, etc. Thus the study by the MHD model is complementary to that by the kinetic model mentioned earlier.

Results from the electromagnetic particle model are now discussed. Figure 2 presents the time history of various field quantities and temperatures in the course of the early formation and the coalescence process with the toroidal field being such that $eB_z/m_ec \equiv \Omega_{et} = 0.2\omega_{pe}$, while Fig. 3 is that with Ω_{et}=1.0ω_{pe}. In Fig. 2(a) both the magnetic field energy and the ion temperature in the direction of coalescence (x) show that, after the early ($t \leq 3\Omega_i^{-1}$) rise which corresponds to the magnetic island formation by tearing, a long relatively dormant period ($t \cong$ 3-22) sets in, followed by a stage ($t \cong$ 22-27) of rapid and huge increase in these oscillatory quantities. It is also evident that after the rapid increase ($t \geq 27$) amplitude oscillations ensue in the coalescence due to overshooting. A similar phenomenon was also observed in the work in Ref. 24. It is to be remarked that all the other quantities shown in Figs. 2(a)-(e) closely follow the pattern of Fig. 2(a) with their characteristic events simultaneously occurring. It is also noted that the amplitude oscillations of the temperatures (T_{ix} and T_{iz} as well as T_{ex} and T_{ez}) and the electrostatic field

energy have a structure of marked double peaks. The valley of the double-peak structure coincides with the peak of the magnetic field energy amplitude. As mentioned in Sec. I, it is important to notice that the rapidness of the increase of each quantity differs and that each quantity explosively increases characterized by a certain definite, but different, index of explosion (i.e., the exponent to the time measured backward from the point of explosion time) until the saturation stage sets in. The early saturation of rise ($t\sim3$) of each quantity in Fig. 2(a)-(e) corresponds to the completion of island formation.[20] The following quiescent period ($3 < t \leq 20$) corresponds to the stage where the formed islands slowly attract each other. The rapid explosive rise ($t \geq 20$) marks the commencement of the explosive coalescence. The following stage of amplitude oscillations correspond to the "breathing"[19] (or pulsations) of coalesced islands (compressional Alfvén oscillations). The induced electric field E_z explosively increases when there is rapid flux reconnection during the explosive coalescence and then oscillates as the magnetic flux in the coalesced island is compressed and decompressed.

Figure 3 shows a similar qualitative trend of the coalescence process when the toroidal field is stronger ($\Omega_{et}=1\omega_{pe}$). There are, however, several differences. Although the double-peak structure still appears in most frames of Fig. 3, some quantities (the electrostatic field energy and T_{iz}, T_{ez}) do not show clear double peaks anymore. In fact, the electrostatic energy does not show systematic amplitude oscillations anymore. The period of the amplitude oscillations and the separation of sub-peak to sub-peak in one double-peak structure are longer.

As the toroidal field is further increased to $\Omega_{et}=2\omega_{pe}$ in this setup, the process of island formation abruptly and qualitatively changes.[12] We called this the threshold phenomenon with the toroidal field. The rate of reconnection for island formation is down by two orders of magnitude and the structure of islands is not coherent but now turbulent.[13] In this case, we never observed that the system went beyond the stage of early island formation (corresponding to $t \leq 3$ in Fig. 2 and 3 cases). So we do not discuss this case in the present paper in any further depth. A case with no toroidal field case $\Omega_{et}=0$ was reported earlier,[20] which will also be closely compared with the present cases ($\Omega_{et}=0.2$ and 1.0).

Let us study the structure of the plasma and fields shortly before and after the completion of island coalescence. Figure 4 exhibits the spatial structure of the magnetic field lines, the toroidal current density J_z, the plasma electron density, the electron flow, the ion flow, and the electric field at t=24Ω_i^{-1}, while Fig. 5 shows that at t=28Ω_i^{-1}. In Fig. 4(a) the island near x=55Δ, y=16Δ is rapidly approaching the other island at x=0 and y=0 pinned by the sheet current gaps. The former island is accelerated by the intense magnetic fields behind it. The density of electrons is sharply peaked just behind the center of the island because of the acceleration [Fig. 4(c)]. Electrons flow mainly along the field lines [Fig. 4(d)], while ions which are left behind the electrons try to catch up with the electrons [Fig. 4(e)]. This sets up an electrostatic field pattern with arrows pointing from the inside to the outside of the island [Fig. 4(f)]. (Note that in the present code the charge of electrons is taken to be positive for a historical reason.)

Figure 5 similarly exhibits the spatial structure of these quantities that appear in Fig. 4. The coalesced island now sits near x=0 and y=16Δ. The electron flow continues in the direction of magnetic fields [Fig. 5(d)]. The ions continue to compress themselves but with a slightly skewed direction (rotation) [Fig. 5(e)].

On the other hand, Fig. 6 presents the case of Ω_{et}=1ω_{pe} just after the coalescence (t=18), corresponding to Fig. 3. (The structure before the coalescence is similar to Fig. 4.) The overall structure after coalescence (t=18) in Fig. 6 is still close to that of Fig. 5, but has a few important differences. The electrons again flow roughly along the magnetic field lines, but shows some kinks. The ion flow shows a rotational motion. The main reason for these is that as the toroidal magnetic field increases, the incompressibility of the plasma increases and upon coalescence the island motion adds a strong component of velocity going like $\mathbf{g} \times \mathbf{B}_t$, where $\mathbf{g}$ is the acceleration of the islands during the coalescence.

Some of the above findings can be given by a qualitative explanation. Since we shall discuss the explosive phase in greater detail later, we pay attention to the amplitude oscillation phase in particular here. Once two currents coalesce, they are bound by the common magnetic flux. The larger coalesced island continues to vibrate. Within the coalesced island the counterstreaming plasma flows cause turbulent flows which dissipate their energy quickly into heat, thereby reducing the amplitude oscillations of temperatures

and fields. As a result, as we shall see, the momentum distribution of plasma electrons and ions exhibit an intense bulk heating and acceleration of the tail. The heating in the poloidal direction (x) is due to adiabatic compression and decompression of the coalesced currents. The eventual bulk heating seems to be a result of turbulent dissipation of counterstreaming instabilities. The heating in the toroidal direction may be due to heating/ acceleration by the inductive toroidal electric field which is several times the classical Dreicer field[25] and due to the $v_{ph} \times B$ acceleration. Examination of some of these processes will be discussed in Sec. IV.

The double peak in the time development of the temperatures occur just before (t=$t_1 \sim 27$) and after (t=$t_3 \sim 29$) the maxima of magnetic fields (t=$t_2 \simeq 28$). In Fig. 7 schematic sequential pictures of plasma dynamical behavior during coalescence are shown. At t=t_1 the magnetic ($J \times B$) acceleration of ions becomes maximum so that the magnetic flux behind the colliding plasma as well as the plasma itself are strongly compressed. This plasma compression causes the first temperature peak at t=t_1. After this maximum acceleration phase ions acquire substantial velocities along the direction of collision so that they overtake the magnetic flux against which ions have been compressed. This results in an expansion phase (t=t_2) of ions, and hence in an adiabatic cooling of the plasma as the magnetic fields obtain maximum values. The process reverses after the maximum of the magnetic fields at t=$t_3 \sim 29\Omega_i^{-1}$, which gives rise to the second peak of the temperature.

The particle acceleration in the high energy tail of ions and electrons may be qualitatively discussed here. The tail formation is probably due to a combination of localized electrostatic field acceleration across the poloidal magnetic field[26] and magnetic acceleration ($v_p \times B$ acceleration), as will be shown in Sec. IV. A plasma and field behavior similar to that shown in Fig. 4 persists up to $t \sim t_1 \sim 27\Omega_i^{-1}$. This is schematized in Fig. 7(a). Found in Fig. 5 is the plasma behavior near t=$t_2 \sim 28\Omega_i^{-1}$ when the maximum of the magnetic field energy is achieved [see Fig. 2(a)]. The schematic of this is shown in Fig. 7(b) (note that in Fig. 5 the spatial scale of the computer plot in the x-direction is different from that in y so that it looks overly prolate). The pattern immediately after (t=$t_3 \sim 29$) is again shown in Fig. 7(c). Electrons are magnetized and are carried away with the accelerating magnetic flux, while bulk ions are accelerated by the $J \times B$ force.

On the other hand, the high energy ions are due to the charge separation created near the compressed flux. The difference of motions between ions and electrons around $t=t_1$ causes a strong localized shock-like electrostatic field, E_L, whose phase propagates with a phase velocity of the structure $v_{ph} = v_x$. Here the mechanism of $v_p \times B$ acceleration is that an electrostatic wave propagating with phase velocity v_p can add energy to a particle that is propagating obliquely to the wave propagation direction by combining the electric acceleration and $v \times B$ acceleration when the particle is trapped in the wave. This $v_p \times B$ acceleration[26-28] causes the formation of high energy particles in the toroidal direction. By this acceleration process, ions and electrons are accelerated to relativistic energies in opposite directions along the toroidal magnetic field.

Results from the magnetohydrodynamic particle models are presented hence. Figure 8 shows the kinetic energy and the reconnected flux upon coalescence as a function of time for the case with ϵ_c=0.85. A theoretical curve $(t_0 - t)^{-4/3}$ is superimposed on the simulation result. During the phase of the rapid increase of reconnected flux ($t \cong 50 - 90\Delta c_s^{-1}$) the simulation result matches reasonably with the theoretical curve. Beyond t=$90\Delta c_s^{-1}$ the increase begins to be mitigated due to a saturation effect (the flux depletion).

Figure 9 displays the case with ϵ_c=0.7. The reconnected flux ψ increases rapidly with $\Delta\psi \propto t^m (m \sim 1.9)$.[15] It is, however, less rapid than the case with ϵ_c=0.85. The released energy is also less in the present case. In Ref. 15 the case with ϵ_c=0.3 was treated, where $\Delta\psi \propto t^m$ with m=1. Thus, it is clear that as ϵ_c increases, the process of reconnection becomes faster, changing from the Sweet-Parker[7] rate to the faster [12,14,15] rate to the explosive rate. It is also noted that the explosive increase of reconnected flux during the coalescence is observed in the MHD simulation as well as in the kinetic simulation discussed earlier. It is to be noted that pulsations are seen that are superimposed on the overall growth of the reconnected flux in Figs. 8 and 9 as well as Figs. 3, 5, and 7 in Ref. 15. The pulsation in Fig. 8 are more irregular than the ones in Fig. 9. In Fig. 8(a) one peak appears at t=$40\Delta c_s^{-1}$ and another at $t \simeq 85\Delta c_s^{-1}$ while smaller peaks appear after the major peak at $t \simeq 95\Delta c_s^{-1}$; in Fig. 9(b) pulsations have a period of $35 \sim 40\Delta c_s^{-1}$, which is of the order of the poloidal Alfvén transit time in the x-direction.

The structure and its evolution of the plasma and magnetic fields during the

coalescence are now examined. The case of ϵ_c=0.7 is shown in Figs. 10-12, while that of ϵ_c=0.85 in Fig. 13. Compared are three time stages: Fig. 10 just about at the beginning of rapid coalescence, Fig. 11 during the continued rapid coalescence, and Fig. 12 after the rapid phase of coalescence. The sequence of coalescence proceeds as follows. The early slight displacement toward each island is shown in Fig. 10(a) at t=20Δ/c_s. When the two islands come in full contact, the magnetic field lines exhibit a pattern similar to that shown in Fig. 1(b) of Ref. 15. At this moment (t=40), the plasma density at the x-point becomes high (about twice as much as the original value) as shown in Fig. 10(c) at the same time the current (J_z) is strongly induced at the x-point as seen in Fig. 10(b). The plasma flow is shown in Fig. 10(d), exhibiting inflows along the x-direction and strong jet outflows along the y-direction making an overall pattern of vortices. The plasma flow in the z-direction is shown in Fig. 10(e): As the x-y flows are set up by the coalescence, the z-direction flow is induced because of the toroidal field. The development so far is qualitatively similar to the case of ϵ_c=0.3 (except that the islands squeeze the plasma in between a little more and the sheet structure is thinner here).

However, later (at t=75) there appear some deviations from the ϵ_c=0.3 case. Figure 11 shows the snapshot of the flux, current, density, flow in the x-y plane, and the flow in the z-direction at t=75Δ/c_s. Note that an x-point-like feature appears at x=64Δ, y=32Δ as well as a marked and rapid density variation in the plasma sheet [see Figs. 11(a) and (c)]: The flow has a very large value near the x-point and inner vortex structure [Fig. 11(d)]. Note also that this (t=75) is the period during which the continuous rapid coalescence goes on. These features were not observed in the case ϵ_c=0.3 (see Fig. 1, Ref. 15), in which the reconnected flux increased linearly in time and in proportion with the square root of the resistivity η ($\Delta\psi \propto \eta^{1/2}t$) and in which the reconnection angle stayed very narrow. Compare with Fig. 3 of Ref. 15.

These signatures are consistent with our hypothesis (a) that the reconnection takes place by the mechanism of Sweet and Parker[7] for coalescence with ϵ_c=0.3. The signatures found in Fig. 11, on the other hand, imply that the reconnection process is not that of Sweet and Parker. It shows instead that (i) the reconnection angle at the x-point has enlarged [Fig. 11(a)]; (ii) a high density spot near the x-point is formed [Fig. 11(c)]; (iii)

the reconnected flux increases faster than the Sweet-Parker process ($\Delta\psi \propto t^m$ with $m \sim 2$). These are consistent with our further hypothesis (b) that the reconnection is through the process of Brunel, Tajima and Dawson[14,15] for coalescence with ϵ_c=0.7. Later (t=160), the system approaches saturation when most of the flux available has reconnected as seen in Fig. 12(a) (at t=140 for this frame) and the high density region has shifted from the x-point to the coalesced island hedge [Fig. 12(c)]. The flow is randomized [Figs. 12(d) and (e)].

Figure 13 presents the pattern of the plasma and fields of the case ϵ_c=0.85, where we see faster and explosive reconnection (Fig. 8). We are advancing our third hypothesis (c) that the coalescence with ϵ_c=0.85 is explosive and this reconnection process is to be characterized by the present paper. See Table II. In frames of Figs. 13(a)-(d) (t=50) one sees the coalescence behavior before it becomes explosive. Although, in Figs. 13(a) and (b), in particular, one can detect some deviation from the Sweet-Parker type for ϵ_c=0.3, it is qualitatively similar to the ϵ_c=0.3 case and the ϵ_c=0.7 case at this stage. In Figs. 13(e) and (f) (t=75), we now see significant deviations in pattern from the cases with less ϵ_c. A much wider reconnection angle than the previous ones is observed in Fig. 13(e). From these observations it can be argued that the widening of the reconnection angle has to be accompanied by fast or explosive coalescence, as suggested by Refs. 12 and 14.

B. Heuristic Derivation of Explosive Coalescence

Some of the observed features of the explosive coalescence detailed in the above can be explained by a simple heuristic theoretical consideration. In the problem of driven fast reconnection Refs. 12 and 14 extracted the essence of the reconnection process that is faster than the Sweet-Parker process. Geometry of magnetic fields here is exemplified by Fig. 11(a). We are primarily concerned with the plasma sheet region (in the neighborhood of x=64Δ and $y \sim$ 20Δ-42Δ). In the vicinity of the sheet region the physics is nearly one-dimensional, that is, the variation of quantities in the y-direction is much less than that in the x-direction. We employ the following equations. First, the magnetic induction

equation, that describes the evolution of the magnetic flux, is

$$\frac{\partial \psi}{\partial t} = -\mathbf{v} \cdot \nabla \psi + \eta \nabla^2 \psi, \tag{1}$$

where ψ is the poloidal flux related to the poloidal magnetic fields (in the x-y plane) $\mathbf{B}_\perp = \nabla\psi \times \hat{z}$. The equation needed next is ordinarily the equation of motion of the plasma and the fluid description of it is $\partial \mathbf{v}/\partial t + \mathbf{v} \cdot \nabla \mathbf{v} = (\nabla \times B) \times B/4\pi\rho - \nabla p/\rho$, where ρ and p are the plasma mass density and the pressure, respectively. When the plasma motion is slow enough to establish a local equilibrium, however, this equation is replaced by the pressure balance equation

$$p_i + B_{iz}^2/8\pi = p_e + B_{ez}^2/8\pi + B_{e\perp}^2/8\pi, \tag{2}$$

where B_z is the toroidal (z) magnetic field and the subscripts i and e refer to the internal and external to the plasma sheet. The third relation is the continuity equation, which under the assumed local equilibrium reads

$$\rho_i u a = \rho_e v L, \tag{3}$$

where the subscripts i and e again indicate the external and internal quantities, v is the incoming flow velocity in the x-direction $v{=}\dot{\psi}/B_{ey}$, a the sheet width (in the x-direction), L the sheet length (in the y-direction), and u is the exhaust (outflow) speed[29] given by

$$u \lesssim B_{ey}/(4\pi\rho_i)^{1/2}. \tag{4}$$

One can identify the left-hand side of Eq. (3) as the particle flux inside the separatrix, while the right-hand side as that outside the separatrix. Equation (1) becomes an ideal MHD equation predominantly determined by

$$\partial\psi/\partial t \simeq v B_y, \tag{5}$$

with $v = \dot{\psi}/B_{ey}$ in the outer region of the plasma sheet, while it takes a form of a diffusion equation in the inner region

$$\frac{\partial \psi}{\partial t} = \eta \nabla^2 \psi \simeq \eta \frac{B_{ey}}{a}. \tag{6}$$

These equations lead to the expressions[14] of temporal behavior of the reconnected flux ψ and the reconnection angle α as

$$\psi = \psi_0 \left(\frac{t}{t_0}\right)^{\rho_i/\rho_e}, \tag{7}$$

and

$$\alpha = \frac{a}{L_*} = \psi/utB_{ey}, \tag{8}$$

where L^* is the time-dependent length of the current sheet. Equations (7) and (8) successfully extracted the main physics of the fast reconnection and explained the driven reconnection simulation results[12,14] as well as the coalescence simulation results with $\epsilon_c \leq 0.7$.[15]

This set of equations can be extended to describe the explosive reconnection. In the explosive process, the local equilibrium, as assumed in the above, can no longer be maintained, but the dynamical pressure equation or the equation of motion as it is has to be employed. In place of Eq. (2) we have

$$\frac{\partial v_x}{\partial t} = \frac{1}{8\pi\rho}\frac{\partial}{\partial x}B_y^2 - \frac{1}{2}\frac{\partial}{\partial x}v_x^2. \tag{9}$$

where we have taken into account the predominant one-dimensionality of the problem in the x-direction and dropped the plasma internal pressure p compared with the dynamical pressure $\frac{1}{2}v_x^2$. The continuity equation Eq. (3) either remains or goes depending upon the compressibility of the plasma. Otherwise, the reduced set of equations as employed in Refs. 13 and 14 are applicable.

To describe the explosive process when the plasma is incompressible, it may be possible to rewrite Eqs. (1) and (9) in terms of the reduced set of MHD equations[30] as

$$\frac{\partial \psi}{\partial t} = \frac{c}{B_z}[\varphi, \psi] + \eta\nabla^2\psi, \tag{10}$$

$$\partial_t \nabla_\perp^2 \varphi = \frac{V_A^2}{cB_z}[\psi, \nabla_\perp^2\psi] - \frac{c}{B_z}[\varphi, \nabla_\perp^2\varphi], \tag{11}$$

where [ ] is the Poisson brackets, φ is the velocity potential $\mathbf{v} = c\hat{z} \times \nabla\varphi/B_z$, and $\nabla_\perp$ is the in-plane gradient.

Let us make an ansatz that in the explosive coalescence the overall evolution of the process is determined by the outer solution and the inner solution has to adjust to the

former. This turns out to be self-consistent and yields theoretical results consistent with the simulation observation. We seek an outer solution to Eqs. (1) and (9). By knowing the existence of the explosive process through our computational work, it is possible to postulate an explicit expression for the flux and velocity in the outer region. It is a special solution for the outer region in a form of separation of variables x and t. Let the functions vary as

$$v_x = \frac{V(x)}{t_0 - t}, \tag{12}$$

$$B_y = \frac{B(x)}{t_0 - t}, \tag{13}$$

$$\psi = \frac{\Psi(x)}{t_0 - t}, \tag{14}$$

$$\varphi = \frac{\Phi(x)}{t_0 - t}, \tag{15}$$

where a one-dimensional model is assumed. By inspection Eqs. (12)-(15) in fact satisfy Eqs. (1) and (9), since all the nonlinear terms are quadratic and the linear terms have the time derivative.

Equations (1) and (9) in the outer region now become

$$\Psi = \Psi' V, \tag{16}$$

$$2V = -\left[(\Psi')^2\right]' - [V^2]', \tag{17}$$

where the primes represent the derivative with respect to x and $4\pi\rho$ is appropriately normalized.

Let us look at a typical behavior of solutions to Eqs. (16) and (17). Take a case in which the left-hand side of Eq. (17) is equated with the first term of the right-hand side (the magnetic acceleration dominant case). Combining with Eq. (16), we obtain

$$(\Psi^2 - \Psi_0^2)^{1/4} = \frac{d\Psi}{dx} \tag{18}$$

where Ψ_0 may be identified with the flux of the center of an incoming island. In particular we may be able to take its value as zero. In this case the solution to Eq. (18) is

$$\Psi(x) = \frac{1}{4}(x - x_0)^2, \tag{19}$$

where x_0 is the center of one of the islands. This solution is valid as long as x is outside of the inner region and satisfies the assumption that we drop the second term on the right-hand side of Eq. (17). Similarly one can obtain the spatial dependence of other quantities V, B, and Φ.

From the temporal behavior of Eqs. (12)-(15) one can cast a prediction on a generic pattern of explosiveness of various quantities upon the explosive coalescence. For example, the magnetic field energy would diverge as

$$B^2 \propto (t_0 - t)^{-2}, \tag{20}$$

from Eq. (13). The electrostatic field can be determined from the massless electron equation of motion

$$E_x - \frac{v_{ez}}{c} \times B_y = 0, \tag{21}$$

along with Ohm's law in the z-direction

$$v_{ez} = \frac{-c}{4\pi ne} \frac{\partial}{\partial x} B_y, \tag{22}$$

where n is the plasma density and the subscript e refers to electron quantities. Combining Eqs. (21) and (22), we obtain

$$E_x = \frac{1}{4\pi n_e} \frac{\partial}{\partial x} (B_y^2/2). \tag{23}$$

Thus, the electrostatic energy would be expected to increase as

$$E_x^2 \propto (t_0 - t)^{-4}. \tag{24}$$

The inductive electric field E_z is related to $v_x \times B_y$ through Ampere's law and thus it would scale as

$$E_z \propto (t_0 - t)^{-2}. \tag{25}$$

The toroidal current J_z is proportional to B_y through Eq. (22) and thus it would scale as

$$J_z \propto (t_0 - t)^{-1}. \tag{26}$$

These estimates of explosiveness of various quantities (the indices of explosion) are to be compared with the observed explosiveness discussed in Fig. 1. The simulation shows (see Fig. 2) in particular that the rise of electrostatic field energy is much faster than that of magnetic energy. The observed indices for these quantities are not far from the values given by Eqs. (24) and (20). If we resort to the reduced version of the continuity equation (3) and assume that ρ_e and ρ_i scale in a similar fashion, we obtain

$$L \simeq (v_{Ai}/v_x)\, a, \tag{27}$$

where $v_{Ai} = B_{ey}/(4\pi\rho_i)^{1/2} \sim$ constant. On the other hand, the magnetic equation (1) in the inner region reads [Eq. (6)]

$$\frac{\partial \psi}{\partial t} = \eta \nabla^2 \psi \sim \frac{\eta}{a} B_y,$$

which yields a scaling of the plasma sheet thickness

$$a \propto (t_0 - t). \tag{28}$$

Using Eqs. (12), (27), and (28), we obtain

$$L \propto (t_0 - t)^2. \tag{29}$$

Comparison of Eqs. (28) and (29) suggests that the originally flat flux structure as shown in Fig. 13(a) similar to the Sweet-Parker[7] configuration ($L \gg a$) makes transition into a structure with increasing a/L, eventually leading to $a/L \sim 0(1)$ similar to the Petscheck[8] configuration. In fact, Fig. 13(e) shows a structure which has a larger reconnection angle at the x-point. A difference of the present explosive process from the case of Ref. 15 and, for the matter of reconnection process itself, Refs. 12 and 14 as well, is that in Refs. 12, 14, and 15 L is proportional to t_0-t and a is held constant, while in the present case L and a scale as Eqs. (28) and (29).

III. Theoretical Model of Explosive Coalescence

As shown in the previous section, the current sheet of nearly one-dimensional structure is formed in the explosive stage of the coalescence instability. As the coalescence proceeds further, the magnetic field structure approaches an x-type (Petsheck type[8]) configuration. We assume that $\frac{\partial}{\partial x} \gg \frac{\partial}{\partial y}, \frac{\partial}{\partial z}$, in which x is the direction of coalescence, while y is the direction of poloidal magnetic field line and z is the direction of plasma current. We treat the external plasma dynamics of the explosive stage as a one-dimensional problem. Toward the end of this section we comment on two-dimensional effects, however. As we shall see, in two-dimension we get essentially the same results as we obtain from the one dimensional model.

We start from the two-fluid model equations of plasma and the Maxwell equations, neglecting the displacement current. We assume the adiabatic law of states for both electrons and ions. The basic equations read as follows:

$$\frac{\partial n_j}{\partial t} + \nabla \cdot (n_j \mathbf{v}_j) = 0 \tag{30}$$

$$m_j n_j \frac{d\mathbf{v}_j}{dt} = n_j e_j \left(\mathbf{E} + \frac{\mathbf{v}_j}{c} \times \mathbf{B} \right) - \nabla p_j, \tag{31}$$

$$\nabla \times \mathbf{B} = \frac{4\pi}{c} \sum_j n_j e_j \mathbf{v}_j, \tag{32}$$

$$\nabla \cdot \mathbf{E} = 4\pi \sum_j n_j e_j, \tag{33}$$

$$\nabla \times \mathbf{E} = -\frac{1}{c} \frac{\partial \mathbf{B}}{\partial t}, \tag{34}$$

$$\frac{\partial p_j}{\partial t} + \mathbf{v}_j \cdot \nabla p_j + \gamma p_j \mathrm{div}\ v_j = 0, \tag{35}$$

where j denotes the species of particles and γ is the ratio of heat capacity which is related to the degree of freedom of the system f as $\gamma=1+\frac{2}{f}$. The appropriate choice of γ in Eq. (35) depends on individual cases and models we use. For example, the explosive process observed in the kinetic simulation showed a strong one dimensional (one directional) acceleration, which gives rise to one degree of freedom of motion $f=1$ and thus to $\gamma=3$. On the other hand, in the MHD simulation, the adiabatic constant γ for electrons was fixed to be 2.

During explosive coalescence, there is no specific scale length. The scale length characterizing the current sheet varies continuously in time without deformation of global structure of current sheet. If one looks at the evolution of the system locally in time, the system undergoes the rapid field and temperature rise, compression of plasma, change of the reconnection angle etc. in a certain specific fashion which was detailed in Sec. II. If one looks at the same system locally in time a little later, the system undergoes these changes with different magnitudes, but still in the same specific fashion. That is, the relations (laws) that govern the explosive coalescence themselves are invariant under the change of time scale. This was the manifestation of the presence of self-similarity in the system during explosive coalescence. This may be called universality in time, as opposed to the conventional universality in space such as in Kadanoff's spin block problem[31] and in Kolmogorov's turbulence spectrum.[32] A similar situation also arises in the general theory of relativity in which the scale factor a plays the Hubble expansion of the universe. Such a physical situation may best be described by self-similar solutions in which scale factors vary continuously. Search for a self-similar solution can often be a quite powerful method, leading to an essentially correct solution to a set of complicated equations where otherwise no manageable solution may be obtained in highly nonlinear situations. In the present paper the self-similarity is not just a theoretical assumption for solution, but it has been demonstrated by the computational experiments as described in the previous section and Table I.

We introduce scale factors $a(t)$ and $b(t)$ as follows,

$$v_{ex} = \frac{\dot{a}}{a}x, \tag{36}$$

$$v_{ix} = \frac{\dot{b}}{b}x, \tag{37}$$

where a dot represents the time derivative. An ansatz is imposed here that the velocities are linear in x. The linear dependence on x of the velocities implies that particles flow in the opposite direction around the center of current sheet, x=0. The scale factors a and b will be determined from the above basic equations. From the continuity equations of electrons and ions, Eq. (31), we obtain

$$n_e = n_0/a, \tag{38}$$

$$n_i = n_0/b, \tag{39}$$

where n_0 is a constant. Equations (38) and (39) show that the densities of ions and electrons are nearly homogeneous in space and vary only in time during coalescence. The self-similar solutions obtained here are local solutions in space whose properties are dominated by the physical process near the current sheet. We therefore neglect the higher order terms in space proportional to x^3 and higher hereafter. The current J_z in the sheet is nearly constant. This means that as n is nearly constant, v_z is also approximately constant in space. Neglecting the term with x^3 in Eq. (32), we obtain

$$\frac{B_0(t)}{\lambda} = \frac{4\pi e n_0}{c}\left(\frac{v_{iz}^{(0)}}{b} - \frac{v_{ez}^{(0)}}{a}\right), \tag{41}$$

where we assumed the magnetic-field B_y varies as $B_y = B_0(t)\frac{x}{\lambda}$, where λ is the magnetic field scale length. This ansatz is consistent with the assumption that the sheet current is (nearly) constant in space.

From the y-component of Eq. (34) and the z-component of equation of motion for electrons Eq. (31) we obtain

$$\dot{B}_0 = 2c\frac{E_{z1}}{\lambda}, \tag{41}$$

$$E_{z1}\frac{x^2}{\lambda^2} + \frac{\dot{a}}{a}\frac{B_0(t)}{\lambda c}x^2 = 0, \tag{42}$$

$$\frac{\partial v_{ez}^{(0)}}{\partial t} = -\frac{e}{m_e}E_{z0}, \tag{43}$$

where

$$E_z = E_{z0}(t) + E_{zl}(t)\frac{x^2}{\lambda^2}. \tag{44}$$

Equations (41) and (42) yield

$$B_0(t) = \frac{B_{00}}{a^2}, \tag{45}$$

where B_{00} is a constant. From the z-component of equation of motion for ions, we get

$$\frac{\partial v_{iz}^{(0)}}{\partial t} = \frac{e}{m_i}E_{z0}. \tag{46}$$

From Eqs. (44) and (46) we have

$$v_{iz}^{(0)} = -\frac{m_e}{m_i}v_{ez}^{(0)}. \tag{47}$$

From Eqs. (43), (47) and (41), we get for $v_{ez}^{(0)}$ and E_z

$$v_{ez}^{(0)} = -\frac{cB_{00}b}{4\pi e n_0 \lambda a^2 \left(\frac{b}{a} + \frac{m_e}{m_i}\right)}, \tag{48}$$

$$E_z = -\frac{B_{00}\dot{a}x^2}{ca^3\lambda} + \frac{m_e c B_{00}}{4\pi n_0 e^2 \lambda}\frac{d}{dt}\left(\frac{b}{a^2\left(\frac{b}{a} + \frac{m_e}{m_i}\right)}\right). \tag{49}$$

Assuming that the electrostatic field E_x varies like $E_x = E_0(t)x/\lambda$, we obtain from Poisson's equation (33)

$$E_0 = 4\pi e n_0 \lambda \left(\frac{1}{b} - \frac{1}{a}\right). \tag{50}$$

Furthermore, the equations of state for electrons and ions give rise to

$$P_e = \frac{P_{0e}}{a^\gamma} - \frac{P_{0e}}{2a^{\gamma+2}}\frac{x^2}{\lambda^2}, \tag{51}$$

$$P_i = \frac{P_{0i}}{b^\gamma} - \frac{P_{0i}}{2b^{\gamma+2}}\frac{x^2}{\lambda^2}. \tag{52}$$

We now go back to the x-component of equations of motion for electrons and ions in order to obtain the basic equations for $a(t)$ and $b(t)$. Substituting Eqs. (50), (51), (52), (45), (38) and (39) into the equation of motion Eq. (31), we finally obtain

$$\ddot{a} = -\omega_{pe}^2\left(\frac{a}{b} - 1\right) - \frac{B_{00}^2 b}{4\pi m_e n_0 \lambda^2 a^3 \left(\frac{b}{a} + \frac{m_e}{m_i}\right)} + \frac{P_{0e}}{m_e n_0 \lambda^2 a^\gamma}, \tag{53}$$

$$\ddot{b} = \omega_{pi}^2\left(1 - \frac{b}{a}\right) - \left(\frac{m_e}{m_i}\right)\frac{B_{00}^2 b^2}{4\pi m_i n_0 \lambda^2 a^4 \left(\frac{b}{a} + \frac{m_e}{m_i}\right)} + \frac{P_{0i}}{m_i n_0 \lambda^2 b^\gamma}, \tag{54}$$

where $\omega_{pe}^2 = \dfrac{4\pi n_0 e^2}{m_e}$ and $\omega_{pi}^2 = \dfrac{4\pi n_0 e^2}{m_i}$. If we neglect the small terms of the order of the mass ratio m_e/m_i, we obtain

$$\ddot{a} = -\omega_{pe}^2\left(\frac{a}{b} - 1\right) - \frac{B_{00}^2}{4\pi m_e n_0 \lambda^2 a^2} + \frac{P_{0e}}{m_e n_e \lambda^2 a^\gamma}, \tag{55}$$

$$\ddot{b} = \omega_{pi}^2\left(1 - \frac{b}{a}\right) + \frac{P_{0i}}{m_i n_0 \lambda^2 b^\gamma}. \tag{56}$$

Furthermore, assuming that the plasma is quasi-neutral $n_i = n_e$, i.e., a=b, by adding Eqs. (55) and (56)

$$\ddot{a} = -\frac{v_A^2}{\lambda^2 a^2} + \frac{c_s^2}{\lambda^2 a^\gamma}, \tag{57}$$

where

$$v_A^2 = \frac{B_{00}^2}{4\pi n_0(m_i + m_e)} \quad \text{and} \quad c_s^2 = \frac{(P_{0e} + P_{0i})}{(m_e + m_i)n_0}.$$

In Eq. (57) the first term of the RHS corresponds to the $J \times B$ term. This is the term that drives magnetic compression (collapse). The second term corresponds to the pressure gradient term. This term may eventually be able to balance the magnetic collapse when γ=3. The condition γ=3 means that the plasma compression takes place in a nearly one-dimensional fashion so that the degree of freedom of the system f becomes unity. When γ=3, we obtain

$$\ddot{a} = -\frac{v_A^2}{\lambda^2 a^2} + \frac{c_s^2}{\lambda^2 a^3}. \tag{58}$$

when γ=2($f = 2$), on the other hand, we obtain

$$\ddot{a} = -\frac{(v_A^2 - c_s^2)}{\lambda^2 a^2}. \tag{59}$$

Once the behavior of the scale factor $a(t)$ is determined from the above equations, we obtain various kinds of physical quantities as follows, in the quasi-neutral plasmas, and neglecting the mass ratio $\left(\frac{m_e}{m_i} \to 0\right)$,

$$B_y = \frac{B_{00}}{a^2}\frac{x}{\lambda} \tag{60}$$

$$E_x = \left(-\frac{m_i}{e_\lambda}\frac{v_A^2}{a^3} + \frac{P_{0e}}{e_\lambda a^4 n_0}\right)\frac{x}{\lambda} \tag{61}$$

$$E_z = -\frac{B_{00}\dot{a}x^2}{ca^3\lambda} - \frac{B_{00}m_e c\dot{a}}{4\pi n_0 e^2 \lambda a^2} \tag{62}$$

$$v_{ez} = -\frac{cB_{00}}{4\pi e n_0 \lambda a} \tag{63}$$

$$v_{ix} = v_{ex} = \frac{\dot{a}}{a}x \tag{64}$$

$$n_i = n_e = \frac{n_0}{a} \tag{65}$$

where the electrostatic field E_x in the quasi-neutral plasmas is determined from the equation of motions for ions, not from Poisson's equations. In Eq. (61), we neglected the term $v_{iz} \times B_y$, because of the order of $\frac{m_e}{m_i}$.

From Eqs. (60) and (61) we find a result that in the explosive phase ($a \to 0$) the electrostatic field $\left[E_x \propto (a^{-3} + a^{-4})\right]$ grows more rapidly than the magnetic field ($B_y \propto a^{-2}$) does. This effect comes into playing a pivotal role for high energy particle production, which will be discussed in Sec. IV.

Now we investigate the global time behavior of coalescence by making use of the first integral of Eq. (58). Equation (58) is rewritten as

$$\ddot{a} = -\frac{\partial V(a)}{\partial a}, \tag{66}$$

where the effective (Sagdeev) potential $V(a)$ is given by

$$V(a) = -\frac{v_A^2}{\lambda^2 a} + \frac{c_s^2}{2\lambda^2 a^2}, \tag{67}$$

where the first term may be reminiscent of the "gravitational potential" while the second of the "centrifugal potential." The schematic graph of the effective potential is drawn in Fig. 14. The value a which satisfies $V(a_1) = 0$ is given by

$$a_1 = \frac{1}{2}\frac{c_s^2}{v_A^2}. \tag{68}$$

The minimum of the potential, $V_{\min}$, obtained from $\partial V/\partial a = 0$ is

$$V_{\min} = \frac{-v_A^4}{2\lambda^2 c_s^2}, \tag{69}$$

at $a{=}2a_1{=}c_s^2/v_A^2$. The potential becomes deeper when the ratio of the kinetic to magnetic energy densities β decreases. This means that the driving force $J \times B$ is dominant compared with the pressure term. The first integral of Eq. (66) is given by

$$\dot{a}^2 = \frac{2v_A^2}{\lambda^2 a} - \frac{c_s^2}{\lambda^2 a^2} + \mathcal{E}, \tag{70}$$

where $\mathcal{E}$ is the initial (Sagdeev) "energy" (dimension: $1/\text{time}^2$) in space of stretching factor a.

$$\mathcal{E} = \dot{a}_0^2 - \frac{2v_A^2}{\lambda^2 a_0} + \frac{c_s^2}{\lambda^2 a_0^2}. \tag{71}$$

As seen from Fig. 14, the explosive magnetic compression corresponds that the scale factor $a(t)$ rapidly changes in time by orders of magnitude and nearly vanishes. We may call this an explosive magnetic collapse. Such an explosive collapse can be realized (i) when the effective potential has a sharp and deep potential well and this means that $\beta = c_s^2/v_A^2$ is very small; (ii) when the initial total energy $\mathcal{E}/2$ is nearly zero. On the other hand, when $\mathcal{E}/2$ is close to $-V_{\min}$, we have oscillations near the potential minimum and no explosive collapse.

Figure 15 shows an example of numerical solutions of Eqs. (53) and (54). The initial conditions in Fig. 15 are: $a = b = 100$, $\dot{a} = 1$, $\dot{b} = -1$, $v_A/\omega_{pe}\lambda = 0.01$, $(P_{0e}/\omega_{pe}^2 m_e n_0 \lambda^2)^{1/2} = 0.01$, and $(P_{0i}/\omega_{pe}^2 m_i n_0 \lambda^2)^{1/2} = 0.01$. The normalizations in Figs. 15(c) and (d) are such that $E_x = b^{-1} - a^{-1}$ for Eq. (50) and $B_y = a^{-2}$ for Eq. (45). Increase of $(P_{0e}/\omega_{pe}^2 m_i n_0 \lambda^2)^{1/2}$ and $(P_{0i}/\omega_{pe}^2 m_i n_0 \lambda^2)^{1/2}$ up to 0.3 does not change the result much. In this example the system is not quasineutral and we observe that b is slowly changing with $b(t)$ roughly proportional to t, while $a(t)$ shows some oscillations. If $\dot{b}(0) = 0$, on the other hand, $b(t) \sim$ constant.

If the total energy is given in Eq. (70), we can find the period T_{os} of nonlinear oscillations by integrating Eq. (70)

$$T_{os} = 2\int_{a_{t1}}^{a_{t2}} \frac{ada}{\left[\mathcal{E}\left(a + \frac{v_A^2}{\mathcal{E}\lambda^2}\right)^2 - \frac{v_A^2}{\mathcal{E}\lambda^2} - \frac{c_s^2}{\lambda^2}\right]^{1/2}}$$

$$= 2\pi \frac{v_A^2}{\mathcal{E}^{3/2}\lambda^2} = 2\pi \mathcal{E}^{-3/2} t_A^{-2}, \tag{72}$$

where a_{t1}, a_{t2} are roots of the equation which gives $\dot{a}$=0:

$$a^2 + \frac{2v_A^2}{\mathcal{E}\lambda^2} a - \frac{c_s^2}{\mathcal{E}\lambda^2} = 0, \tag{73}$$

and $t_A = \lambda/v_A$. In the limit of $\mathcal{E} \to -V_{\min}$, we find the minimum period $T_{\min}$ as

$$T_{\min} = 2\pi \beta^{3/2} t_A. \tag{74}$$

Equation (72) indicates that the period T_{os} of nonlinear oscillations becomes longer when $\mathcal{E}$ tends to zero.

Let us examine the time history of various physical quantities based on the qualitative time behavior of $a(t)$ derivable from the effective potential $V(a)$. The magnetic field energy is proportional to B_y^2, which is given by

$$B_y^2 = \frac{B_{00}^2}{a^4}\left(\frac{x}{\lambda}\right)^2.$$

If the scale factor a becomes smaller, B_y^2 must increase. The maximum is given by

$$\frac{\partial B_y^2}{\partial t} = 0,$$

which yields $\dot{a}$=0, namely a=a_{t1}. After the maximum, B_y^2 decreases again and reaches minimum at a=a_{t2}. The oscillatory behavior of the magnetic field energy is schematically drawn in Fig. 16. The period of the oscillation is given by Eq. (72).

The electrostatic field E_x is given by Eq. (61). The time history of the electrostatic field energy, which is propositional to E_x^2, is analyzed by investigating

$$\frac{\partial E_x^2}{\partial t} = 0.$$

This condition is equivalent to

$$\mathcal{E}_0 = 0, \tag{75a}$$

or

$$\frac{\partial \mathcal{E}_0}{\partial t} = 0, \tag{75b}$$

where $\mathcal{E}_0(t) = -\frac{m_i}{e\lambda}\frac{v_A^2}{a^3} + \frac{P_{0e}}{e\lambda n_0 a^4}$. The first condition $\mathcal{E}_0$=0 occurs at a=a_3 = $P_{0e}/m_i n_0 v_A^2 \cong c_s^2/v_A^2$. The second condition $\frac{\partial \mathcal{E}_0}{\partial t}$ gives two conditions, namely

(i) $\dot{a} = 0$, which occurs at a=a_{t1}, a_{t2}

(ii) $a = a_4 = \frac{4}{3}\frac{P_{0e}}{m_i n_0 v_A^2} \cong \frac{4}{3}\frac{c_s^2}{v_A^2} = \frac{4}{3}\beta.$

The above considerations give us the schematic time history of the electrostatic field energy E_x^2 as drawn in Fig. 17. Figure 17 indicates a triple-peak structure in the electrostatic field energy. When the plasma β is small, a_3 and a_{t1} are close. In this

case, the triple-peak structure in the electrostatic field energy would become double-peak structure. The maximum value of the electrostatic field, $E_{\max}$, achieved at $a{=}a_4$ is given by

$$E_{\max} = \frac{1}{4}\left(\frac{3}{4}\right)^3 \frac{m_i}{e\lambda}\frac{v_A^8}{c_s^6}\frac{x}{\lambda} \cong 0.1\frac{m_i}{e\lambda}\frac{v_A^2}{\beta^3}\frac{x}{\lambda}. \tag{76}$$

The induced electric field E_z is given by Eq. (62), which shows that E_z becomes zero, when $\dot{a}{=}0$. E_z changes its sign around $\dot{a}{=}0$ because $\dot{a}{=}0$ is the point where the magnetic field achieves maximum or minimum.

Next, the time behavior of ion temperature T_{ix} is examined. In the early stage of coalescence, the plasma should be adiabatically compressed. However, as the magnetic field energy increases near the peak and approaches the peak, the ion flow energy becomes dominant over the thermal energy. From the consideration that v_x^2 gives maximum or minimum, namely $\dfrac{\partial v_x^2}{\partial t} = 0$, we find two conditions for the extrema; (i) $v_x = 0$, which gives $\dot{a}$, (ii) $\dfrac{\partial v_x}{\partial t} = 0$, which gives

$$a\ddot{a} = \dot{a}^2. \tag{77}$$

When the explosive coalescence takes place ($\mathcal{E}{=}0$), we estimate the condition (77) as

$$a = a_5 \simeq \frac{2}{3}\frac{c_s^2}{v_A^2} = \frac{2}{3}\beta.$$

After $a{=}a_5$, the kinetic energy must decrease, which means that the plasma is in the state of colliding phase, see Fig. 7. The above considerations give us the schematic time history of the ion temperature, which is shown in Fig. 18. Figure 18 shows a double-peak structure in the ion temperature. In the limit of quasi-neutrality, we can estimate the dominant term governing the explosive phase where the adiabatic compression is predominant. The temperature T is given by $T{=}P/n$, while the dominant term in pressure changes in time as $P \sim a^{-5}$ when $\gamma{=}3$, $P \sim a^{-4}$ when $\gamma{=}2$, while $n \sim a^{-1}$. Therefore we find

$$T = P/n \simeq \frac{1}{a^4}\ (\gamma = 3), \tag{78a}$$

$$\simeq \frac{1}{a^3}\ (\gamma = 2). \tag{78b}$$

We investigate in more detail the explosive phase of the coalescence in a case where we can neglect the effect of plasma pressure: it only acts as a saturation mechanism. However, if we take γ=2, the pressure does not take the role of a saturation mechanism as seen in Eq. (59). In the explosive phase, therefore, we can neglect the second term on the right-hand side of Eq. (58);

$$\ddot{a} = -\frac{v_A^2}{\lambda^2 a^2}. \tag{79}$$

Furthermore, we need a second condition for explosive collapse, namely the initial total energy $\mathcal{E}$ must be close to zero. For example, if the oscillation period of magnetic energy is of the order of the transit Alfvén time $t_A = \lambda/v_A$, we can estimate the total energy $\mathcal{E}$ by making use of Eq. (72) as

$$T_{os} = 2\pi \mathcal{E}^{-3/2} t_A^{-2} \approx t_A, \tag{80}$$

which gives

$$\mathcal{E} \sim \frac{(2\pi)^{2/3}}{t_A^2}. \tag{81}$$

The solution of Eq. (79) with small $\mathcal{E}$ is given by

$$a(t) \cong \left(\frac{9}{2}\right)^{1/2} \left(\frac{v_A}{\lambda}\right)^{2/3} (t_0 - t)^{2/3} + 0(\mathcal{E}), \tag{82}$$

where we neglect the order of $\mathcal{E}$ and t_0 is the explosion time. Once the solution $a(t)$ is given by Eq. (82), we can find the various physical quantities as follows, which is valid in the explosive phase of the coalescence;

$$v_x = v_{ix} = v_{ex} = -\frac{2}{3}\frac{x}{(t_0 - t)}, \tag{83}$$

$$n = n_i = n_e = \left(\frac{2}{9}\right)^{1/3} \frac{\lambda^{2/3} n_0}{v_A^{2/3}(t_0 - t)^{2/3}}, \tag{84}$$

$$E_x = -\frac{2}{9}\frac{m_i}{e}\frac{x}{(t_0 - t)^2}, \tag{85}$$

$$B_y = \left(\frac{2}{9}\right)^{2/3} \frac{B_{00}\lambda^{1/3} x}{v_A^{4/3}(t_0 - t)^{4/3}}, \tag{86}$$

$$E_z = \frac{2}{3}\left(\frac{2}{9}\right)^{2/3} \frac{B_{00}\lambda^{1/3}x^2}{v_A^{4/3}c(t_0-t)^{7/3}} + \frac{2}{3}\left(\frac{2}{9}\right)^{1/3} \frac{B_{00}c}{\omega_{pe}^2\lambda^{1/3}v_A^{2/3}(t_0-t)^{5/3}}. \tag{87}$$

The explosion time t_0 is related to the initial condition. From Eq. (83) we find the initial velocity v_{x0} at t=0 as

$$v_{x0} = \frac{\dot{a}_0}{a_0}x = -\frac{2x}{3t_0}, \tag{88}$$

where a_0, $\dot{a}_0$ are the initial values of a, $\dot{a}$ at t=0. From Eq. (88) we find

$$t_0 = -\frac{2}{3}\frac{a_0}{\dot{a}_0}(>0), \tag{89}$$

where $\dot{a}_0$ must be negative when magnetic collapse occurs. On the other hand, a_0 and $\dot{a}_0$ are related to the initial total energy as

$$\mathcal{E} = \dot{a}_0^2 - \frac{2v_A^2}{\lambda^2 a_0} \tag{90}$$

when the pressure term is neglected. If $\mathcal{E} \simeq 0$, we obtain from Eqs. (89) and (90)

$$t_0 \simeq \frac{\sqrt{2}}{3}a_0\sqrt{a_0}t_A. \tag{91}$$

Combining Eqs. (85) and (86), we find that in the explosive phase the electrostatic field $E_x \propto (t_0-t)^{-2}$ more rapidly grows compared with the magnetic field $B_y \propto (t_0-t)^{-4/3}$. This fact becomes important when we consider the high energy particle production by E_x during the explosive phase of the coalescence.

Let us compare the theoretical results obtained here for the explosive phase with the computer simulation results. The global structure of the magnetic field energy, electrostatic field energy, and ion temperature in the x-direction observed in the simulation is well explained by the theoretical model obtained here. Especially, the double-peak structure in the ion temperature and the triple-peak structure in the electrostatic field energy are also observed in the simulation (see Figs. 2 and 3). Table I summarizes the results of comparison of the explosion indeces between the theory and the collisionless simulation.

In Table I we show the index m of explosiveness [the exponent to the time $(t_0 - t)^{-m}$]. Table I shows a good agreement between simulation and theory in the electrostatic

energy. When the toroidal field becomes comparable with the poloidal field ($B_t/B_p = 1$ case), there appears two-dimensional motion, plasma rotational motion (Fig. 6), which makes a more complex electrostatic field configuration. When $B_t/B_p = 1$, the magnetic time behavior of field energy also deviates from the one-dimensional analysis for the same reason. For the ion temperature we find its explosiveness from Eq. (77) as

$$T \sim \frac{1}{a^4} \sim \frac{1}{(t_0 - t)^{8/3}} \tag{92}$$

when γ=3. The above scaling also is close to the results obtained in the simulation, except for the case of $B_t/B_p = 1$. If we use γ=2, we find from Eq. (78)

$$T \sim \frac{1}{a^3} \sim \frac{1}{(t_0 - t)^2}, \tag{93}$$

which may correspond to two-dimensional adiabatic compression. (However, we still have some small discrepancy from the simulation.) In Fig. 1, the electrostatic field energy, magnetic field energy, and ion temperature are well explained by the one-dimensional model of the explosive collapse.

Comments are made on two-dimensional effects. As shown in the one-dimensional analysis, the neglect of electron mass ($m_e/m_i \to 0$) is justified. The current J_z is maintained only by the electrons. Furthermore, the magnetic force for ions are also of the order of the mass ratio. We introduce four scale factors $a(t)$, $b(t)$, $c_1(t)$ and $d(t)$ as follows

$$\begin{aligned} v_{ix} &= \frac{\dot{a}}{a}x, \\ v_{iy} &= \frac{\dot{b}}{b}y, \\ v_{ex} &= \frac{\dot{c}_1}{c_1}x, \\ v_{ey} &= \frac{\dot{d}}{d}y. \end{aligned} \tag{94}$$

From the continuity equation we find

$$n_i = \frac{n_0}{ab},$$

$$n_e = \frac{n_0}{c_1 d}. \tag{95}$$

From the Maxwell equation, we obtain

$$v_{ez} = -\frac{cc_1 d}{4\pi e n_0 \lambda}\left(\frac{1}{c_1^2} - \frac{1}{d^2}\right). \tag{96}$$

Similarly we get from Poisson's equation

$$\varphi_0 = \frac{\lambda_1\lambda_2}{\lambda_1+\lambda_2} 4\pi e n_0 \left(\frac{1}{ab} - \frac{1}{c_1 d}\right), \tag{97}$$

where

$$\varphi = -\frac{\varphi_0(t)}{2}\left(\frac{x^2}{\lambda_1} + \frac{y^2}{\lambda_2}\right). \tag{98}$$

The magnetic field is given by

$$B_x = \frac{B_{00}}{d^2}\frac{y}{\lambda_1},$$

$$B_y = \frac{B_{00}}{c^2}\frac{x}{\lambda_2}. \tag{99}$$

From the equations of motion for electrons and ions we finally obtain for a, b, c_1, and d

$$\ddot{a} = \omega_{pi}^2\left(\frac{\lambda_2}{\lambda_1+\lambda_2}\right)\left(\frac{1}{b} - \frac{a}{c_1 d}\right) \tag{100}$$

$$\ddot{b} = \omega_{pi}^2\left(\frac{\lambda_1}{\lambda_1+\lambda_2}\right)\left(\frac{1}{a} - \frac{b}{c_1 d}\right) \tag{101}$$

$$\ddot{c}_1 = -\omega_{pe}^2\left(\frac{\lambda_2}{\lambda_1+\lambda_2}\right)\left(\frac{c_1}{ab} - \frac{1}{d}\right) - \frac{v_{Ae}^2}{\lambda^2}\left(\frac{d}{c_1^2} - \frac{1}{d}\right) \tag{102}$$

$$\ddot{d} = -\omega_{pe}^2\left(\frac{\lambda_1}{\lambda_1+\lambda_2}\right)\left(\frac{d}{ab} - \frac{1}{c_1}\right) + \frac{v_{Ae}^2}{\lambda^2}\left(\frac{1}{c_1} - \frac{c_1}{d^2}\right) \tag{103}$$

where

$$v_{Ae}^2 = \frac{B_{00}^2}{4\pi n_0 m_i}.$$

If we assume the quasi-neutrality ($n_i = n_e$) in the above equations, which imposes that "Wronskian" equal to zero, ab=$c_1 d$, we find

$$\ddot{c}_1 = -\frac{v_A^2}{\lambda^2}\left(\frac{d}{c_1^2} - \frac{1}{d}\right), \tag{104}$$

$$\ddot{d} = \frac{v_A^2}{\lambda^2}\left(\frac{1}{c_1} - \frac{c_1}{d^2}\right). \tag{105}$$

These equations were first derived by Imshenik and Syrovatskii.[33] As noted in their paper, in the limit of $t \to t_0$ we have approximately

$$c_1 \simeq (t_0 - t)^{2/3} \quad \text{and} \quad d \approx \text{constant}.$$

This just reduces to the one-dimensional results discussed in the above. Roseneau also obtained self-similar two-dimensional solution.[34]

Finally, comments on the effect of non-quasineutrality are due. In the explosive phase, we can neglect the effect of pressure terms in Eq. (55) and Eq. (56):

$$\ddot{a} = -\omega_{pe}^2\left(\frac{a}{b} - 1\right) - \frac{v_{Ae}^2}{\lambda^2 a^2}, \tag{106}$$

$$\ddot{b} = \omega_{pi}^2\left(1 - \frac{b}{a}\right). \tag{107}$$

From the analysis of numerical calculations of Eqs. (106) and (107), we can conclude that b is slowly varying in time during the variation of a. Therefore if we use the result of $b \simeq b_0$=const. in Eq. (106), we find the effective potential $V(a)$ as

$$\ddot{a} = -\frac{\partial V(a)}{\partial a},$$

$$V(a) = \omega_{pe}^2\left(\frac{a^2}{2b_0} - a\right) - \frac{v_{Ae}^2}{\lambda^2 a}, \tag{108}$$

The schematic graph of the potential is given in Fig. 19. Here we write the effective potential including the effect of plasma pressure. The curve that incorporates the pressure effect is shown as the broken line near a=0. Figure 19 shows a second minimum at $a=a_{\min}$ which is caused by the effect of charge separation. When the $J \times B$ force dominates, the charge separation effect is unimportant. Such is the case of explosive phase of coalescence (where charge neutrality is maintained to a good degree). However, after the coalescence in the late stage of amplitude oscillations, the $J \times B$ force becomes weaker. Then the charge separation may become important. In this stage electrons can be trapped and oscillate in the potential well near the second minimum in Fig. 19. The electrostatic field oscillations

are similar to the dipole oscillations near the current sheet. Such dipole oscillations may be able to radiate the electromagnetic wave ($\omega \sim \omega_{pe}$ or ω_{pi}), if the plasma is not evanescent. The simulation results obtained show certain high frequency oscillations in the frequency range of $\omega \sim \omega_{pe}, \omega_{LH}$ (the lower hybrid frequency). The detailed comparison will be reported elsewhere. Once other effects such as the two-dimensional curvature effect are included, it might be possible to have additional minima in the effective potential and thus for the system to be temporarily trapped in the potential well and exhibit pulsations that are found in Figs. 8 and 9.

IV. Explosive Acceleration

We have found that in the magnetic collapse the electrostatic field can be explosively generated and can grow more rapidly than the magnetic field. The explosiveness of the electrostatic field $E_x \sim (t_0 - t)^{-2}$, and magnetic field $B_y \sim (t_0 - t)^{-4/3}$ agree well with the results obtained in the simulations (see Figs. 1-3). As shown later, the kinetic simulation finds that, in the explosive phase, ions and electrons are simultaneously accelerated in the z-direction, opposite each other. When a particle moves across the magnetic field driven by the electrostatic field E_x, the particle can be accelerated in a direction (z-direction) perpendicular both to the electric field (x-direction) and the poloidal magnetic field (y-direction). This acceleration mechanism was considered by Sugihara et al.[27] and Dawson et al.[28] On the other hand, Sagdeev and Shapiro[26] discussed the same physics from another point of view, namely the large amplitude wave damping due to trapped electrons. These previous works are applicable to the cases in which the large amplitude electrostatic waves can propagate across the static magnetic field. In the explosive phase during magnetic collapse, a similar situation can be realized; now both the magnetic field and electrostatic field can vary in time and space.

Figures 20 and 21 show the distribution functions of electrons and ions in the coalescence simulation from the electromagnetic particle code. In Fig. 20 we compare the distribution of electrons and ions before the explosive coalescence and the distribution after that. The upper four frames [(a), (b), (e), (f)] are the distribution functions just before the coalescence, while the lower frames [(c), (d), (g), (h)] are after the coalescence. It is clear

that the distribution functions have very rapidly changed during the explosive coalescence and strong heating of ions in the coalescence direction has occurred during this time. It is also observed that there is a very small but energetic population of electrons has been created in the z-direction perhaps due to the inductive acceleration. A similar pattern is observed in the ion distribution in the z-direction with the appropriate parity difference because of the charge difference between electrons and ions. Electrons are accelerated in the negative z-direction, while ions are in the positive z-direction. Ions are strongly heated in the x-direction, i.e., in the direction of coalescence, as seen in Fig. 20(g) in comparison with Fig. 20(e). (In these frames a maximum or minimum of the distribution corresponds to the extrema of the horizontal abssissa. Therefore, in Fig. 20(e), for example, although we do not see a clear tail, there exist electron hot tails up to ± 12mc). In Fig. 21 we replotted the data from Figs. 20(h) and 20(f) in logarithmic scales. From Figs. 21(a) and (b) it is learned that the ion distribution in the z-direction has three regimes, the bulk, the hot part, and the highly accelerated part. The hot distribution goes like either $f_i(p_z) \propto e^{p_z/p_{zo}}$ or $p_z^{-3.5}$. From Fig. 21(c) the hot electron distribution in the z-direction goes like $f_e(p_z) \propto e^{-p_z/p_{zo}}$ or hot Gaussian. It should be noted that the explosive coalescence produces extremely energetic ions which form a relatively flat and long plateau: Some particles are accelerated with kinetic energies up to their rest mass. These observations may be explainable in the following discussion.

In this section we study particle acceleration by examining a test particle motion under the explosive electromagnetic fields during magnetic collapse. By means of the electromagnetic fields, Eqs. (85), (86) and (87), we obtain the equations of motion of a test ion

$$\frac{dv_x}{dt} = \frac{eE_{x0}}{m_i}\frac{x}{(t_0-t)^2} - \frac{eB_{y0}}{m_i c}\frac{xv_z}{(t_0-t)^{4/3}}, \tag{109}$$

$$\frac{dv_z}{dt} = \frac{e\hat{E}_{z0}}{m_i}\frac{x^2}{(t_0-t)^{7/3}} + \frac{9}{2}\frac{e\hat{E}_{z0}c^2 v_A^{2/3}}{m_i\lambda^{2/3}\omega_{pe}^2(t_0-t)^{5/3}} + \frac{eB_{y0}}{m_i c}\frac{\dot{x}x}{(t_0-t)^{4/3}} \tag{110}$$

where we define

$$E_{x0} = 2m_i/9e \quad , \quad \hat{E}_{z0} = \frac{2}{3}\left(\frac{2}{9}\right)^{2/3}\frac{B_{00}\lambda^{1/3}}{cv_A^{4/3}} = \frac{2}{3}\frac{B_{y0}}{c}. \tag{111}$$

Particular attention is paid to a particle which is driven by the electrostatic field in Eq. (109). Such a particle can be accelerated in the x-direction without Larmor motion. One may say that the particle has an infinite Larmor radius, while background plasma particles have (nearly) zero Larmor radius and zero acceleration. Even if the velocity v_z is small in the initial stage, v_z can increase by $ev_x \times B_y/c$ of Eq. (110) through the increase of v_x. This acceleration can proceed till E_x becomes comparable with $v_z B_y/c$. After that the particle takes a gyrating motion. The maximum velocity $v_{z\,\mathrm{max}}$ by this acceleration mechanism is expressed as

$$v_{z\,\mathrm{max}} = \frac{cE_x}{B_y}. \tag{112}$$

The dynamo force $ev_x B_y/c$ that accelerates the particle in the z-direction depends on the sign of charge, so that the electron and the ion are accelerated in directions opposite to each other. The maximum velocity depends neither on the charge nor on the mass of the particle as in Eq. (112). Therefore the maximum energy of ions is larger than that of electrons by the mass ratio.

We examine equations of motion (109) and (110) for the test particle. Transforming the time t to $\tau = t_0 - t$, we find

$$\frac{dv_x}{d\tau} = -\frac{eE_{x0}}{m_i}\frac{x}{\tau^2} - \frac{eB_{y0}}{m_i c}\frac{xv_z}{\tau^{4/3}}, \tag{113}$$

where we used the relation $E_{z0} = 2B_{y0}/3c$, as we have seen in Eq. (111). We also find

$$\frac{dv_z}{d\tau} = -\frac{eB_{y0}}{m_i c}\left[\frac{2}{3}\frac{x^2}{\tau^{7/3}} + \frac{\delta}{\tau^{5/3}} - \frac{x}{\tau^{4/3}}\frac{dx}{\delta\tau}\right], \tag{114}$$

where $\delta = 9c^2 v_A^{2/3}/2\omega_{pe}^2 \lambda^{2/3}$. Since ions are accelerated mostly by the electrostatic field E_x ($eE_x \gg ev_z B_y/c$), ions are approximately determined by

$$\frac{dv_x}{d\tau} = -\frac{eE_{x0}}{m_i}\frac{x}{\tau^2}. \tag{115}$$

The solution of Eq. (115) is given as

$$x = c_1\tau^{2/3} + c_2\tau^{1/3},$$

$$v_x = \dot{x} = \frac{2}{3}c_1\tau^{-1/3} + 1/3c_2\tau^{-2/3}, \tag{116}$$

where c_1 and c_2 are determined from initial conditions

$$c_1 = 3\left(v_0 t_0^{1/3} - x_0 t_0^{-2/3}\right),$$

$$c_2 = 3\left(x_0 t_0^{-1/3} - v_0 t_0^{2/3}\right). \tag{116}$$

Equation (116) implies that the ions with non-zero c_1 and c_2 can be explosively accelerated in the x-direction.

By means of the solution (116) we find the solution for v_z from Eq. (114)

$$v_z = \frac{eB_{y0}}{m_i c}\left(\frac{c_2^2 + 3\delta}{2\tau^{2/3}} + \frac{c_1 c_2}{\tau^{1/3}}\right). \tag{118}$$

Equation (117) indicates that the ion with a particular initial condition, $c_1 \neq 0$, can be explosively accelerated in the z-direction. The dominant term in Eq. (118) is the first term with c_2 in the limit of $\tau \to 0$. From Eq. (114) with condition $E_{z0} < v_x B_y/c$ we obtain $\delta \ll c_2$ and from Eq. (109) with condition $E_x > v_z B_y/c$ we have $c_2 \lesssim v_A^{8/3}/2\Omega_i^2\lambda^{2/3}$ in this limit. The ions which satisfy the relation $\delta \ll c_2 \lesssim v_A^{8/3}/2\Omega_i^2\lambda^{2/3}$ can be accelerated by the $v_p \times B$ mechanism. The second relation $c_2 \lesssim v_A^{8/3}/2\Omega_i^2\lambda^{3/2}$ corresponds to $E_x \gtrsim \frac{v_z}{c}B_y$. This means that the ion can be initially accelerated without gyrating motion. The ion with $c_2 \lesssim v_A^{8/3}/2\Omega_i^2\lambda^{2/3}$ can be accelerated until the explosion time ($\tau \to 0$), because the electrostatic field always exceeds the magnetic force $v_z B_y$.

If we consider a test electron, we find the velocity in the z-direction as

$$v_{ze} = -\frac{eB_{y0}}{m_e 0}\left(\frac{d_1^2}{2}\tau^{\mu-1/3} + \frac{3}{2}\delta\tau^{-2/3} + d_1 d_2 \tau^{-1/3} + \frac{d_2^2}{2}\tau^{-\mu-1/3}\right) \tag{119}$$

where

$$\mu = (1 + 8m_i/9m_e)^{1/2},$$

$$d_1 = \mu^{-1}\left[v_0 t_0^{(1-\mu)/2} - \frac{(1-\mu)}{2}x_0 t_0^{-(1+\mu)/2}\right],$$

$$d_2 = \mu^{-1}\left[\frac{(\mu+1)}{2}x_0 t_0^{(\mu-1)/2} - v_0 t_0^{(1+\mu)/2}\right].$$

The constants d_1 and d_2 are determined from the initial conditions for the electron. Since $\mu \gg 1$, the main term in Eq. (119) is the last one. From this it is learned that the electrons with nonzero d_2 can be explosively accelerated in the direction opposite to the ions.

The ions can be accelerated during the explosion period, while the electrons can be detrapped from the electrostatic field at $\tau=\tau_A$ before the explosion time

$$\tau_A = \left[\frac{2}{d_z^2}\left(\frac{eE_{x0}}{m_e}\right)\left(\frac{eB_{y0}}{m_e c}\right)^{-2}\right]^{3/(1-3\mu)}. \tag{120}$$

At $\tau=\tau_A$ the electrons gain the maximum velocity $V_{ze}^{\max}$ given by

$$\begin{aligned} V_{ze}^{\max} &= -\frac{d_2^2}{2}\left(\frac{eB_{y0}}{m_e c}\right)\tau_A^{-\mu-1/3} \\ &= -\frac{d_2^2}{2}\left(\frac{eB_{y0}}{m_e c}\right)\left[\frac{2}{d_2^2}\left(\frac{eE_{x0}}{m_e}\right)\left(\frac{eB_{yo}}{m_e c}\right)^{-2}\right]^{\frac{-1-3\mu}{1-3\mu}}. \end{aligned} \tag{121}$$

This is of the order of cE_x/B_y as already indicated by Eq. (112). The degree of explosiveness ($v_{ez} \propto \tau^{-\mu-1/3}$) of electron acceleration z-direction is higher than that of ion ($v_{iz} \propto \tau^{-2/3}$): the index of explosion for ions is $\mu + 1/3 > 2/3$.

We compare theory with the results of simulation. Figure 20 shows the distribution functions for ions and electrons in the early stage of the coalescence and after the coalescence. In the z-direction high energy tail particles (both electrons and ions) are observed, accelerated in the opposite directions. The maximum velocity is estimated by use of the maximum value E_x given by Eq. (76) at $a = 4/3c_s^2/v_A^2$. At this value of the magnetic field B_y is given as

$$B_y\left(a = \frac{4}{3}\frac{c_s^2}{v_A^2}\right) = B_{00}\left(\frac{3v_A^2}{4c_s^2}\right)^2\frac{x}{\lambda}. \tag{122}$$

Therefore we obtain $v_{\max}$ as

$$v_{\max} = \frac{cE_x}{B_y} = \frac{3v_A^4}{16(\Omega_i\lambda)c_s^2}, \tag{123}$$

where $\Omega_i = eB_{00}/m_i c$. The maximum velocity normalized to the ion thermal velocity is obtained by use of Eq. (123) as

$$\left(\frac{v_{\max}}{v_{Ti}}\right)^2 = 0.035\left(\frac{v_A}{\Omega_i\lambda}\right)^2\left(\frac{v_A}{v_{Ti}}\right)^2\beta^{-2}. \tag{124}$$

In the simulation we observed $E_x/B_y \sim 0.71$. If the velocity is relativistic, the maximum momentum is given by

$$\frac{p_{\max}}{m_0 c} = \frac{(E_x/B_y)}{\left[1-\left(\frac{E_x}{B_y}\right)^2\right]^{1/2}}, \tag{125}$$

This expression says that if $E_x/B_y \sim 0(1)$, $p_{\max}$ becomes $\gamma m_0 c$. The simulation value $E_x/B_y \sim 0.71$ implies $p_{\max} \approx m_0 c$ and this is observed in the z-direction of ion distribution function. As was earlier, when E_x becomes $v_z B_y/c$, particles begin gyrating again, thus prohibiting $1-(E_x/B_y)^2$ from becoming negative. We need more study to determine what exact value of E_x/B_y will be at saturation.

V. Discussion

An explosive reconnection process associated with the nonlinear evolution of the coalescence instability has been found in the electromagnetic particle simulation and the MHD particle simulation. The explosive coalescence is a process of magnetic collapse, in which we find the magnetic and electrostatic field energies and ion temperatures explode toward the explosive time t_0 as shown in Table I and Fig. 1. Single-peak, double-peak, and triple-peak structures of magnetic, temperature, and electrostatic energy, respectively, are observed in the simulation as overshoot amplitude oscillations. The heuristic model[14] is extended to this explosive coalescence in order to theoretically explain the basic process. Since the explosive coalescence exhibits self-similarity in time, we have searched for a self-similar solution to the two-fluid plasma equations. The self-similar solutions have been solved through the scale factors. The scale factors are governed by the equation of motion in a Sagdeev potential which consists of the "gravitational" attractive term and the "centrifugal" repulsive term. Our theory has produced the indices of explosion (exponent of the time) in agreement with our simulation results. For the coalescence to go explosive, the plasma β ratio has to be low, i.e., the $j \times B$ force overwhelms the pressure force ∇p, and the "total energy" $\mathcal{E}$ has to be close to zero. The structure of the Sagdeev potential indicates that the temporal evolution of the magnetic energy shows a maximum and a minimum in one oscillation period. It also indicates that the temporal behavior of the electrostatic energy entails that a maximum splits into a second maximum and two minima shown in

Fig. 17. On the other hand the ion temperature has a structure that a maximum splits into a minimum as shown in Fig. 18. The coalescence accompanies explosive acceleration of ions and electrons. When the coalescence goes explosive, the electrostatic field diverges faster than the magnetic field, which contributes to efficient acceleration of particles. Once particles are trapped by the magnetic front (this may be called as a shock wave or magnetosonic wave), then they keep accelerated explosively, leading to a production of very energetic particles.

We summarize the temporal behavior of reconnected flux for various values of the current peakedness parameter ϵ_c in Table II. At ϵ_c=0 no chain of islands initially exists and the system is unstable against the linear tearing instability,[35] which grows exponentially with the linear growth rate γ_L. At a small value of ϵ_c=0.3 the chain of islands is unstable against the coalescence mode, which grows exponentially in the early linear regime with linear growth rate that is independent of the resistivity η.[17] In its later nonlinear regime flux grows linearly in time with the coefficient proportional to $\eta^{1/2}$. At a moderately large value of ϵ_c=0.7 the nonlinear regime exhibits a faster time dependence of $t^m (m \geq 1)$. Its coefficient is approximately porportional to $\eta^{1/2}$. At a still larger value of ϵ_c=0.85 reconnected flux can go explosively as we have discussed. We have presented in this article a theoretical construct of the explosive coalescence process that we found through our numerical simulation. The theory is macroscopic in nature, neglecting the detailed development of the singular layer.

A. Applications

There are many applications of the coalescence instability and its nonlinear stages to fusion plasmas as well as to astrophysical plasmas. A certain class of Doublet plasma evolution[36] sometimes is characterized as the coalescence process. A compact torus formation involves the coalescence of islands and ion rings.[3] The tokamak internal disruption may be characterized by the m=1 resistive kink mode.[5] This process has been recently studied by Bussac et al.[37] and called the "half-coalescence". They found that the island slips and rotates as it reconnects. This is similar to the coalescence. See Fig. 22. In Fig. 22(a) the coalescence is shown in which two same-sense currents tend to attract each

other. When there is a strong toroidal magnetic field present, two islands rotate during the process. This rotation is related to the tilting.[6] The "half-coalescence"[37] is shown in which two currents are in the opposite sense indicated by a dot and a cross in Fig. 22(b), and they repel each other. In a way similar to the coalescence, two islands rotate as well as repel each other. By this repulsion together with reconnection the revulsion of the inner island could take place.

An application of the coalescence process to a certain class of the impulsive phase of solar flares has been suggested.[19] Many aspects of the impulsive phase of the solar flare observed by Forrest et al.[38] are naturally explained by this mechanism. Later Nakajima et al.[39] found that a flare of different type was also well explained by the present mechanism. The explosive coalescence process naturally accounts for (i) the rapid and explosive nature of impulsive solar flares; (ii) the necessity to convert a substantial portion of magnetic energy into kinetic energy because of the large amount of observed energy release; (iii) the observed motion of attraction of two objects; (iv) the amplitude oscillations observed in the bands of γ-ray, x-ray and microwaves; and (v) the observed signatures in the profile of amplitude oscillations of the above. The explosive acceleration of particles upon the coalescence may explain some of high energy particle production during the active flare phase. It is encouraging to know that a recent experiment[40] observed a fast reconnection similar to Ref. 14.

B. Contact with Other Phenomena

The explosive process we described in the present article possesses in common a kind of properties found in much wider and general areas of physics. That is, the explosive phase of the coalescence (until it saturates or bounces back) lacks any characteristic time scale, a form of temporal universality. Some of this type of phenomena occur in plasma physics. In this subsection we speculate on a possible link with various areas of plasma physics.

One may compare the present explosive coalescence in two dimensions with the tokamak major disruption. The explosive process we find in the coalescence instability is characterized by singular functions of time with a pole (or a branch point) at the explosion

time $(t_0-t)^{-m}$. The tokamak major disruption has been modeled as nonlinear evolution of unstable tearing[41] and/or resistive kink[42] modes (mainly the m=2, n=1 mode and m=3, n=2) and their destabilization of other beat modes such as the m=5, n=3 mode and its coupling to higher m and n's. It is interesting to extract from their numerical simulation[43] that the toroidal voltage approximately scales as $(t_0-t)^{-2}$ toward the disruption time t_0 to our best fit (Fig. 5 of Ref. 43). The toroidal voltage is related to E_z in the present paper, which has power exponents of 7/3 and 5/3 according to Eq. (87), close to 2. Furthermore, it is of interest to note that we are unable to make a good fit of type $(t_0-t)^{-m}$ with the kinetic energy growth in Fig. 3 of Ref. 43: Rather, the exponent γ itself explodes as $(t_0-t)^{-2}$ to our best fit, suggesting an approximate functional form of $\exp[(t_0-t)^{-1}]$ for the kinetic energy. That is, we may conclude from this study of Fig. 3 of Ref. 43 that the singularity of the temporal explosion of the major disruption is characterized by an essential singularity. In their model the electrostatic potential ϕ and the magnetic flux ψ obey equations of quadratic nonlinearity. With single helicity calculations it seems not possible for us to construct temporal functions with an essential singularity. However, with multiple helicities interacting with each other it may be possible to argue that a strongly developed turbulence which is established by a cascade of many higher order beat modes gives rise to an essential singularity in the temporal behavior: secondary processes yielding $(\varphi,\psi)\propto(t_0-t)^{-2}$, tertiary processes (beats of beats)$\propto(t_0-t)^{-3}$, quartic processes $\propto(t_0-t)^{-4}$,.... With a certain combinatorial arrangement which depends on individual dynamics of turbulence, one sums up the entire energy as $\sum_{n=0}^{\infty}C_n(t_0-t)^{-n}$, where C_n's are coefficients; the analytic property of such a function may be generically related to that of $\exp[(t_0-t)^{-1}]$. [Mathematically speaking, perhaps fortuitously, it might be stated that the analytic property of solutions to an ordinary differential equation of second order at a regular singular point is similar to the analytical property of the present explosive process in two dimensions, while that at an irregular singular point (or confluence of two regular ones) to that of the major disruption of three-dimensional nature.] It may be argued, on the other hand, that the toroidal voltage is not a result of a multiplicative process but an additive one, thus resulting in the temporal behavior of a pole type as in two dimensions.

Felber discussed[44] self-similar solutions of a Z-pinch collapse. In his work a single

current is pinched by its own magnetic field and the magnetic collapse is bounced back by the plasma pressure. Such collapse and bouncing back were observed to be nearly self-similar in experiments.[45] One may further compare the present process with the explosive heating observed in a computer simulation of plasma heating by the ion cyclotron resonant heating method.[46] In Ref. 46 it is observed that the magnetic energy $(\delta B)^2$ diverges as $(t_0 - t)^{-3/2}$. In this cyclotron resonance heating simulation $\delta B \propto E$ (electric field). It is also observed that the primary pump with mode number ± 7 indices a strongest "side-band" mode with mode number ± 2 with weaker "side bands" with ± 5 and ± 9. Therefore, the most unstable mode 2 might be governed by $\dot{E}_2 \propto |E_7|^2 E_2$ while other modes are of a quadratic nonlinear type $\dot{E}_n \propto E_{n'} E_{n-n'}$. Combining these three mode equations we may describe the fields as $\partial^3 E/\partial t^3 \propto E^4$, which yields $E \propto (t_0 - t)^{-3/4}$.

It may be of interest to compare the present process of the magnetic collapse with other physical processes. An obvious counterpart to this is the electrostatic collapse of plasma waves[47,48] in which the process proceeds explosively in two or three dimensions.[49] Note that the magnetic collapse can occur in a quasi-one dimensional case.

Acknowledgments

We would like to thank many of our colleagues for helpful discussions and encouragement during the past several years. These include Drs. F. Brunel, A. Bhattacharjee, J.N. Leboeuf, H. Nakajima, R. Sugihara, W. Horton, and J.M. Dawson. This work is supported by the U.S. Department of Energy, contract DE-FG05-80ET-53088, and the National Science Foundation Grants ATM-82-14730 and ATM-85-06646.

References

1. L.A. Artsimovich, Nucl. Fusion **12**, 215 (1972).
2. D.A. Baker and W.E. Quinn, in *Fusion*, ed. by E. Teller (Academic, New York, 1981) Ch. 7.
3. J.M. Finn and R.N. Sudan, Nucl. Fusion, **22**, 1443 (1982).
4. B.B. Kadomtsev, Sov. J. Plasma Phys. **1**, 389, (1975).
5. B. Coppi, R. Galvao, R. Pellat, M.N. Rosenbluth, and P.H. Rutherford, Sov. J. Plasma Phys. **2**, 533 (1976).
6. M.N. Rosenbluth and M.N. Bussac, Nucl. Fusion **19**, 489 (1979).
7. P.A. Sweet, in *Electromagnetic Phenomena in Cosmic Physics* (Cambridge Univ. Press, London, 1958), p. 123; E.N. Parker, J. Geophys. Res. **62**, 509 (1957).
8. H.E. Petschek, Proc. AAS-NASA Symposium on Physics of Solar Flares (NASA SP-50, 1964) p. 425.
9. E.R. Priest, *Solar Magnetohydrodynamics* (Reidel, Dordrecht, 1981).
10. C.T. Russell, in *Magnetic Reconnection in Space and Laboratory Plasmas* ed. by E. Hones (American Geophysical Union, Washington, D.C., 1984) p. 124.
11. E. Hones, ed. *Magnetic Reconnection in Space and Laboratory Plasmas* (AGU, Washington, D.C., 1984).
12. T. Tajima, in *Fusion-1981* (International Centre for Theoretical Physics, Trieste, 1982) p. 403.
13. T. Sato and T. Hayashi, Phys. Fluids **22**, 1189 (1979).
14. F. Brunel, T. Tajima, and J.M. Dawson, Phys. Rev. Lett. **49**, 323 (1982).
15. A. Bhattacharjee, F. Brunel, and T. Tajima, Phys. Fluids **26**, 3332 (1983).
16. J.M. Finn and P.K. Kaw, Phys. Fluids **20**, 72 (1977).
17. P.L. Pritchett and C.C. Wu, Phys. Fluids **22**, 2140 (1979).
18. V.M. Fadeev, I.F. Kvartskawa, and N.N. Komarov, Nucl. Fusion **5**, 202 (1965).
19. T. Tajima, F. Brunel, and J.-I. Sakai, Ap. J. **245**, L45 (1982).
20. J.N. Leboeuf, T. Tajima, and J.M. Dawson, Phys. Fluids **25**, 784 (1982).
21. A.T. Lin, J.M. Dawson, and H. Okuda, Phys. Fluids **17**, 1995 (1974).

22. A.B. Langdon and B. Lasinski, in *Methods of Computational Physics* (Academic, New York, 1976) p. 327.

23. J.N. Leboeuf, T. Tajima, and J.M. Dawson, J. Comput. Phys. **31**, 379 (1979); F. Brunel, J.N. Leboeuf, T. Tajima, J.M. Dawson, M. Makino, and T. Kamimura, J. Comput. Phys. **43**, 268 (1981).

24. J.N. Leboeuf, F. Brunel, T. Tajima, J. Sakai, C.C. Wu, and J.M. Dawson, in *Magnetic Reconnection in Space and Laboratory Plasmas* ed. by E. Hones (American Geophysical Union, Washington, D.C., 1984), p. 282.

25. H. Dreicer, Phys. Rev. **115**, 238 (1959).

26. R.Z. Sagdeev and V.D. Shapiro, JETP Lett. **17**, 279 (1973).

27. R. Sugihara and Y. Midzuno, J. Phys. Soc. Jpn. **47**, 1290 (1979).

28. J.M. Dawson, V.K. Decyk, R.W. Huff, I. Jaeckert, T. Katsouleas, J.N. Leboeuf, B. Lemberge, R.M. Martinez, Y. Ohsawa, and S.T. Ratliff, Phys. Rev. Lett. **50**, 1455 (1983).

29. F. Brunel and T. Tajima, Phys. Fluids **26**, 535 (1983).

30. H. Strauss, Phys. Fluids **19**, 134 (1976).

31. L.P. Kadanoff, W. Götze, D. Hamblen, R. Hecht, E.A.S. Lewis, V.V. Palciauskas, M. Rayl, J. Swift, D. Aspnes, and J. Kane, Rev. Mod. Phys. **39**, 395 (1967).

32. A.N. Kolmogorov, Comput. Rend. Acad. Sci. USSR **30**, 301 (1941). [Sov. Phys.-Uspekhi **10**, 734 (1968)].

33. V.S. Imshennik and S.I. Syrovatskii, Sov. Phys. JETP **25**, 656 (1967) [Zh. Ek. Teor. Fiz. **52**, 990 (1967)].

34. P. Roseneau, Phys. Fluids **22**, 848 (1979).

35. H.P. Furth, J. Killeen, and M.N. Rosenbluth, Phys. Fluids **6**, 1054 (1963).

36. T.H. Jensen and F.W. McClain, J. Plasma Phys. **28**, 495 (1982).

37. M.N. Bussac, R. Pellat, J.L. Soule, and M. Taggar, Phys. Lett. **105A**, 51 (1984).

38. D.J. Forrest and E.L. Chupp, Nature (Letters) **305**, 291 (1983).

39. H. Nakajima, T. Tajima, F. Brunel, and J.-I. Sakai, in *Proc. Course and Workshop on Plasma Astrophysics* (Varenna, Italy, ESA, 1984) p. 193.

40. E. Sevillano and F.L. Ribe, in *Magnetic Reconnection in Space and Laboratory Plasmas* ed. by E. Hones (AGU, Washington, D.C., 1984) p. 313.
41. B. Carreras, M.N. Rosenbluth, and R. Hicks, Phys. Rev. Lett. **46**, 1131 (1981).
42. J.F. Drake and R.G. Kleva, in *Proc. 1985 Sherwood Theory Conference* (University of Wisconsin, Madison, Wisconsin, 1985), paper 2Q-2.
43. P.H. Diamond, R.D. Hazeltine, Z.A. An, B.A. Carreras, and H.R. Hicks, Phys. Fluids **27**, 1449 (1984).
44. F.S. Felber, Phys. Fluids **25**, 643 (1982).
45. F.J. Mayer and D.J. Tanner, KMS Fusion Report KMSF-U865 (1979); F.S. Felber and R. Decoste, Phys. Fluids **21**, 520 (1978).
46. T. Tajima and J.M. Dawson, Nucl. Fusion **20**, 1129 (1980).
47. V.E. Zakharov, Sov. Phys. JETP **35**, 968 (1972).
48. K. Nishikawa, Y.C. Lee, and C.. Liu, Comments Plas. Phys. **2**, 63 (1975)..
49. M.V. Goldman and D.W. Nicholson, Phys. Rev. Lett. **41**, 406 (1978).

Figure Captions

1. Explosive increase of field energies and temperature during the coalescence of two magnetic islands: EM particle simulation results. For the case $\Omega_{et} = 0.2$. Other parameters are given in Sec. II. Toward the same explosion time $t = t_0 = 27(\Omega_i^{-1})$, the magnetic energy B^2 (a), electrostatic energy E_L^2 (b), and the ion temperature in the x-direction T_{ix} (c) diverge as $(t_0 - t)^{-8/3}$, $(t_0 - t)^{-4}$, and $(t_0 - t)^{-8/3}$, as shown in (d), (e), and (f), respectively. [We took $B_0^2 \sim 1.6 \times 10^5$, $E_{Lo}^2 \sim 7.5 \times 10^3$, and $T_{ixo} \sim 0.85$ for the pre-explosive phase values; see Figs. 1(a)-(c)].
2. Temporal profiles of particle and field quantities for the coalescence process obtained from the EM particle simulation. $\Omega_{et} = 0.2\omega_{pe}$. (a) The thick line represents the magnetic energy, the thin one the ion temperature in the x-direction. (T_{ix} at t=0 was 0.5). (b) Electrostatic field energy in time. (c) Ion temperature in the z-direction. (d) Electron temperature in the x-direction. (e) Electron temperature in the z-direction (f) Inductive electric field (E_z) in time.
3. Temporal profiles of particle and field quantities for the coalescence obtained from the EM particle simulation with $\Omega_{et} = 1.0$. (a) The thick line for the magnetic energy, thin line for ion temperature in x. (b) Electrostatic energy. (c) Ion temperature in z. (d) Electron temperature in x. (e) Electron temperature in z. (f) Inductive electric field E_z.
4. Spatial structure of plasma and fields before coalescence with $\Omega_{et} = 0.2$ at $t = 24\Omega_i^{-1}$ obtained from the EM particle simulation. (a) Magnetic field lines. (b) Current density J_z. (c) Plasma density (d) Electron flow in the $x - y$ plane. (e) Ion flow in the $x - y$ plane (f) Electric fields in the $x - y$ plane.
5. Spatial structure of plasma and fields during coalescence with $\Omega_{et} = 0.2$ at $t = 28\Omega_i^{-1}$ obtained from the EM particle simulation. (a)-(f) as indicated for Fig. 4.
6. Spatial structure of plasma and fields during coalescence with $\Omega_{et} = 1$ at $t = 18\Omega_i^{-1}$ obtained from the EM particle simulation. (a)-(f) as indicated for Fig. 4.
7. Schematic sequence of snapshots of the plasma and electric and magnetic fields during the coalescence process.
8. Temporal profiles of the fluid energy (a) and the reconnected flux (b) for $\epsilon_c = 0.85$

obtained from the MHD particle simulation. A solid line in (b) is a theoretical curve discussed in Sec. III.

9. Temporal profiles of the fluid energy (a) and the reconnected flux (b) for $\epsilon_c = 0.7$ obtained from the MHD particle simulation. A solid line in (b) is a fit to the simulation data.
10. Spatial structure of plasma and fields "before" coalescence with $\epsilon_c = 0.7$ obtained from the MHD particle simulation. (a) Magnetic field lines at $t = 20\Delta c_s^{-1}$. (b) Toroidal current density J_z contours. (c) Plasma density. (d) Plasma flow velocity. (e) Plasma z-direction flow velocity contours. (b)-(e) at $t = 40\Delta c_s^{-1}$: Solid lines correspond to above-average contours and dotted ones to below-average.
11. Spatial structure of plasma and fields "during" coalescence with $\epsilon_c = 0.7$. (a)-(f) as indicated for Fig. 10. (a)-(e) at $t = 75\Delta c_s^{-1}$.
12. Spatial structure of plasma and fields "after" coalescence with $\epsilon_c = 0.7$. (a)-(f) as indicated for Fig. 10. (a) at $t = 140\Delta c_s^{-1}$ and (b)-(e) at $t = 160\Delta c_s^{-1}$.
13. Spatial structure of plasma and fields "before" and "during" coalescence with $\epsilon_c = 0.85$. (a) Magnetic field lines. (b) Plasma density contours. (c) Plasma flow velocities. (d) Current density (J_z) contours. (a)-(d) at $t = 50\Delta c_s^{-1}$. (e) Magnetic field lines. (f) Plasma density contours. (e) and (f) at $t = 87.5\Delta c_s^{-1}$.
14. The Sagdeev potential for the scale factor of the explosive coalescence with the eigenvalue given by $\mathcal{E}/2$ and turning points a_{t1} and a_{t2}.
15. Numerical solution of the scale factors a, b in Eqs. (53) and (54) in (a) and (b). Normalized electric and magnetic fields are also plotted in (c) and (d). (e) with different initial conditions with $\dot{a}(0) < 0$ shows a case of amplitude oscillations.
16. The schematic temporary behavior of the magnetic field energy constructed from the Sagdeev potential.
17. The schematic temporal behavior of the electrostatic field energy constructed from the Sagdeev potential.
18. The schematic temporal behavior of the ion-temperature in the x-direction (in the direction of coalescence) constructed from the Sagdeev potential.
19. The Sagdeev potential for the scale factor including the plasma pressure and the

non-neutral effects.

20. Distribution functions of electrons and ions "before" [(a)-(d)] and "after" [(e)-(h)] coalescence from EM simulation. (a)-(d) at $t = 24\Omega_i^{-1}$ and (e)-(h) at $t = 28\Omega_i^{-1}$. (a) and (e) the electron velocity distribution in the x-direction. (b) and (f) the electron velocity distribution in the z-direction. (c) and (g) the ion velocity distribution in the x-direction. (d) and (h) the ion velocity distribution in the z-direction. Note that unit for velocities on the left frames is $\omega_p\Delta$, while those on the right is c. The electron momenta are measured in $m\omega_p\Delta$ (or $M\omega_p\Delta$ for ions) on the left, while those on the right in mc (or Mc for ions).
21. The logarithmic distribution functions of ions and electrons after the explosive coalescence. The data are taken from Figs. 20(h) and 20(f).
22. Schematic comparison between the coalescence of the same sense currents (a) and the "half-coalescence" of the opposite sense currents (b). Currents are in the same sense (crosses) for the coalescence, while they are in the different sense (a dot and a cross) with suggested rotation by arrows in addition to the attractive and repulsive reconnection.

Indices of Explosion [exponents to the $1/(t_0 - t)$] During Coalescence

		$\Omega_{et} = 0$ $L_x \times L_y$ $= 128 \times 32$ (see Ref. 26) [NB: $L_x \times L_y$ $= 256 \times 32$ many islands]	$\Omega_{et} = 0.2\omega_{pe}$ $L_x \times L_y$ $= 128 \times 32$	$\Omega_{et} = 1.0$ $L_x \times L_y$ $= 128 \times 32$	$\Omega_{et} = 2.0$ $L_x \times L_y$ $= 128 \times 32$ No formation of islands
Magnetic Energy	(S)	8/3	8/3	2	
B^2	(T)	8/3	8/3	2*	N/A
Electrostatic Energy	(S)	4	4		
E_L^2	(T)	4	4	4	N/A
Ion Temperature in	(S)	8/3	8/3	3	
x-direction	(T)	8/3	8/3	2	N/A
T_{ix}					
Explosive Time	(S)	$24.3\Omega_i^{-1}$	$27\Omega_i^{-1}$	$19\Omega_i^{-1}$	N/A
t_0					
Compressional Alfvén Oscillation Period		$6.3\Omega_i^{-1}$	$6.0\Omega_i^{-1}$	$8.8\Omega_i^{-1}$	N/A
τ_{os}					

* incompressibility is assumed. Derivation from observation might be due to plasma rotation in $\Omega_{et} = 1$ case.

S is for simulation results and T for theory.

TABLE I

Coalescence and Current Peakedness (ϵ_c)

ϵ_c	0	0.3	0.7	0.85
Process	Sheetpinch tearing instability	Slow Coalescence Sweet-Parker process	Fast Coalescence	Explosive Coalescence
Recon. flux $\Delta\psi$	$\mathbf{e}^{\gamma_L t}$ $\gamma_L \propto \eta^{3/5}$	$\eta^{1/2}t$	$\eta^{1/2}t^m$ $(m \geq 1)$	$\eta^0/(t_0 - t)^{4/3}$

TABLE II

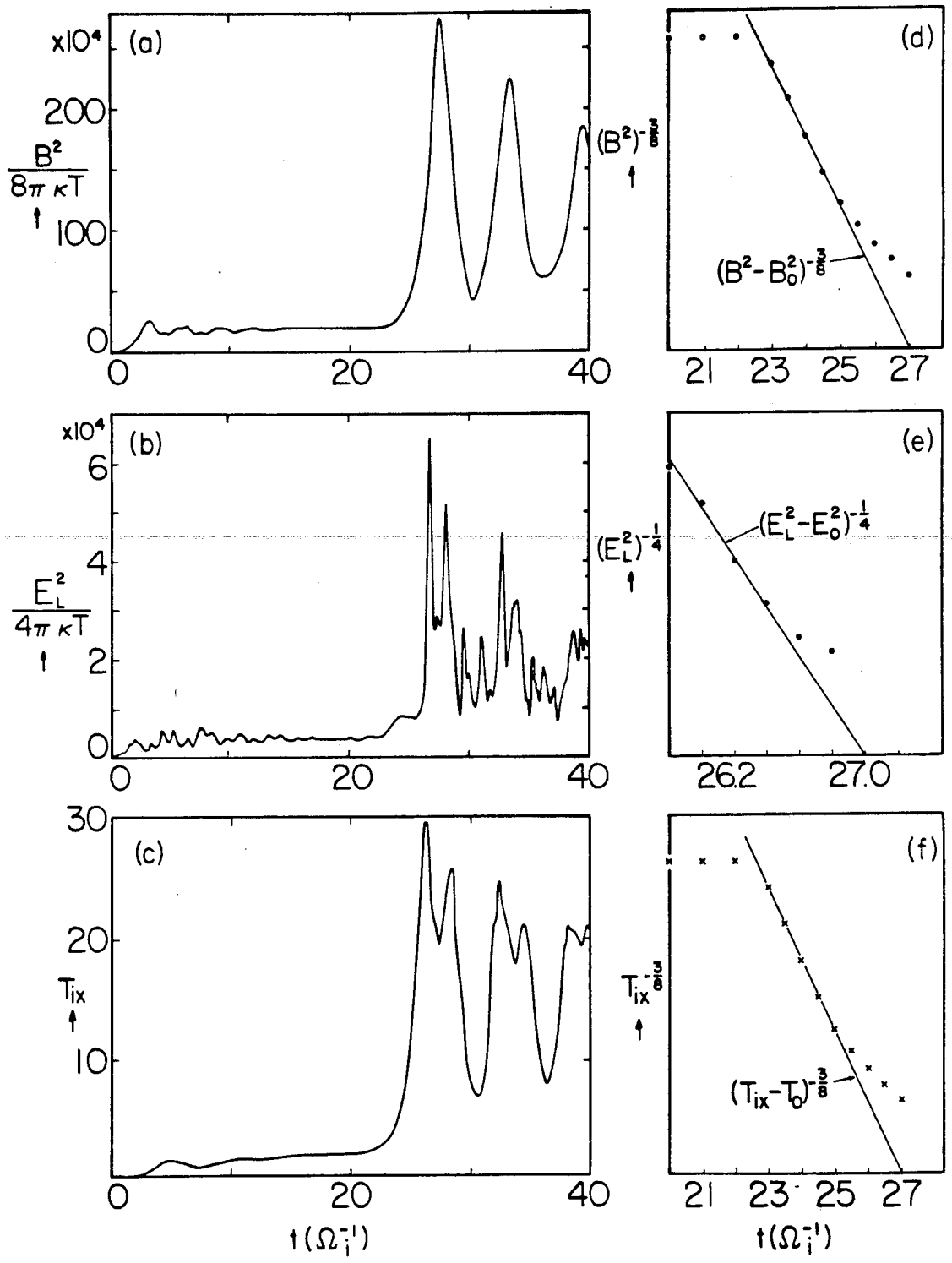
(a)
x10⁴
200
100
0
$\frac{B^2}{8\pi\kappa T}$
0
20
40
(b)
x10⁴
6
4
2
0
$\frac{E_L^2}{4\pi\kappa T}$
0
20
40
(c)
30
20
10
T_{ix}
0
20
40
$t(\Omega_i^{-1})$
(d)
$(B^2)^{-\frac{3}{8}}$
$(B^2-B_0^2)^{-\frac{3}{8}}$
21
23
25
27
(e)
$(E_L^2)^{-\frac{1}{4}}$
$(E_L^2-E_0^2)^{-\frac{1}{4}}$
26.2
27.0
(f)
$T_{ix}^{-\frac{3}{8}}$
$(T_{ix}-T_0)^{-\frac{3}{8}}$
21
23
25
27
$t(\Omega_i^{-1})$

Fig. 1

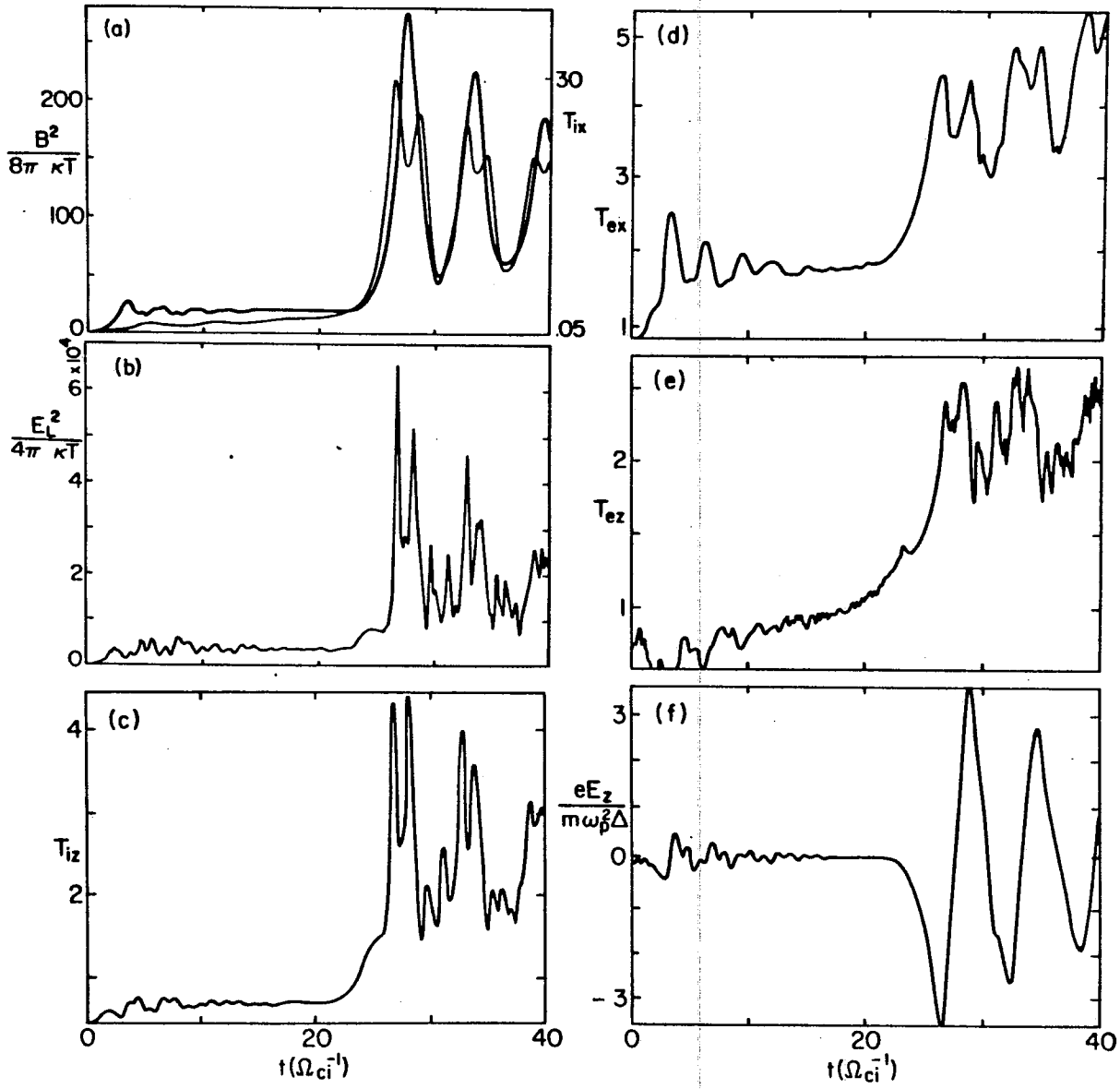
(a)
200
$\frac{B^2}{8\pi\ \kappa T}$
100
0
30
T_{ix}
.05
(b)
$\frac{E_L^2}{4\pi\ \kappa T}$
$\times 10^{-4}$
6
4
2
0
(c)
T_{iz}
4
2
0
20
40
$t(\Omega_{ci}^{-1})$
(d)
5
3
1
T_{ex}
(e)
2
1
T_{ez}
(f)
3
0
-3
$\frac{eE_z}{m\omega_p^2\Delta}$
0
20
40
$t(\Omega_{ci}^{-1})$

Fig. 2

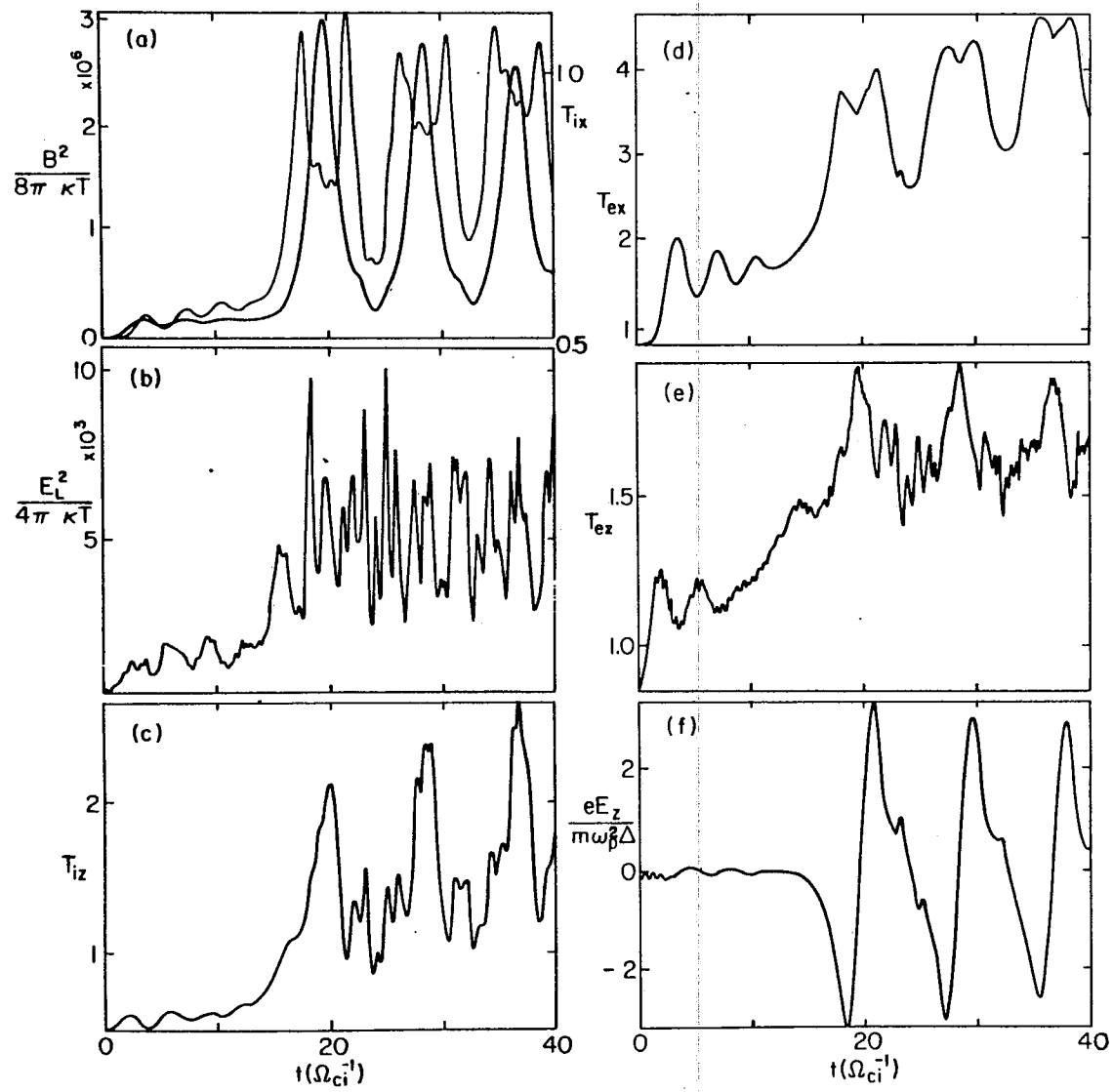
(a)
(b)
(c)
(d)
(e)
(f)
$\frac{B^2}{8\pi\ \kappa T}$
x10^6
T_{ix}
$\frac{E_L^2}{4\pi\ \kappa T}$
x10^3
T_{iz}
T_{ex}
T_{ez}
$\frac{eE_z}{m\omega_p^2\Delta}$
t(Ω_ci^-1)
t(Ω_ci^-1)

Fig. 3

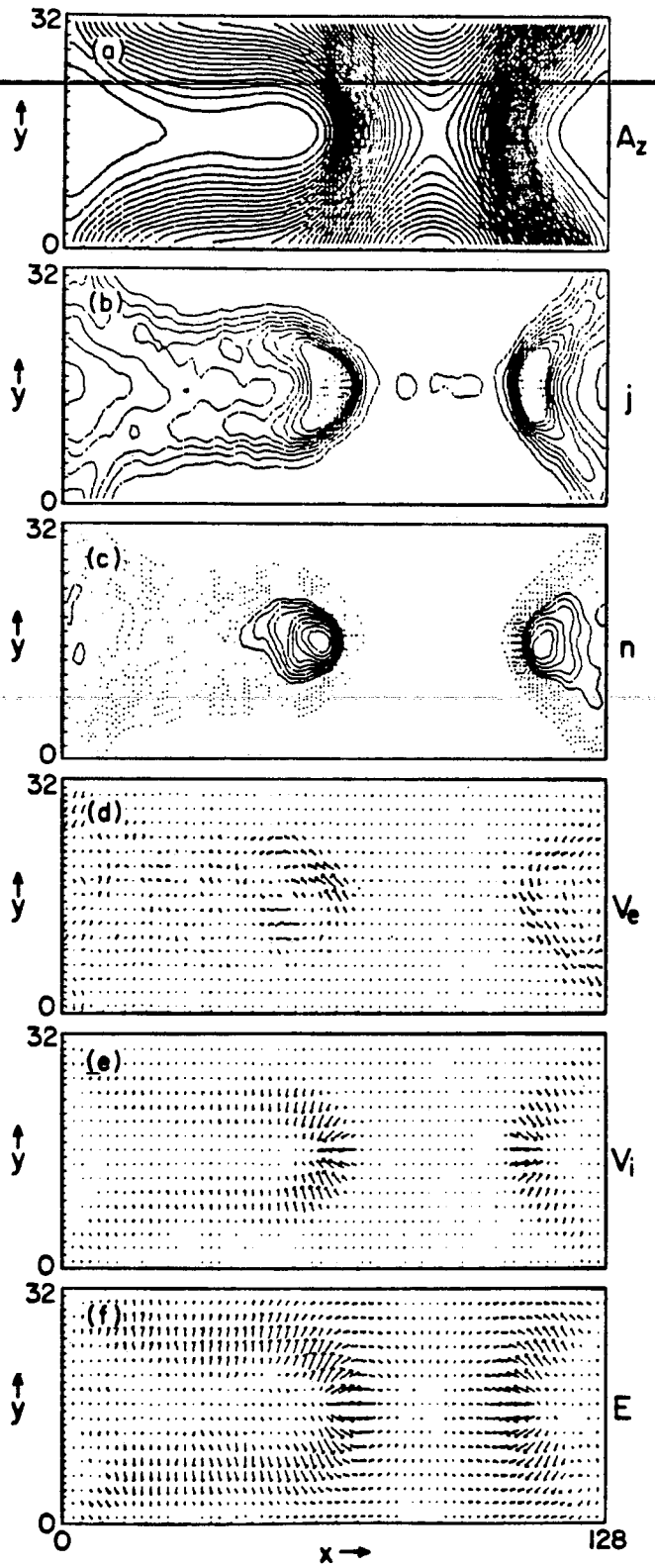

Fig. 4

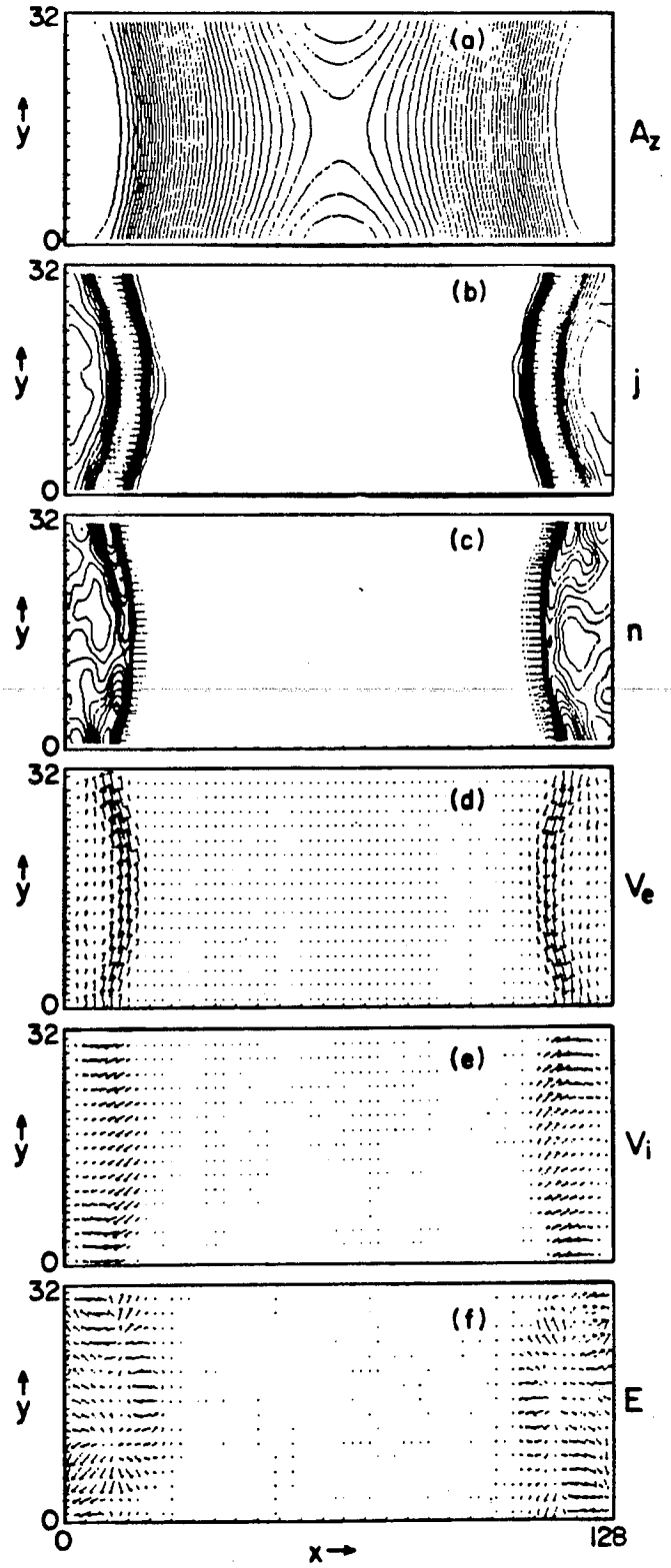

Fig. 5

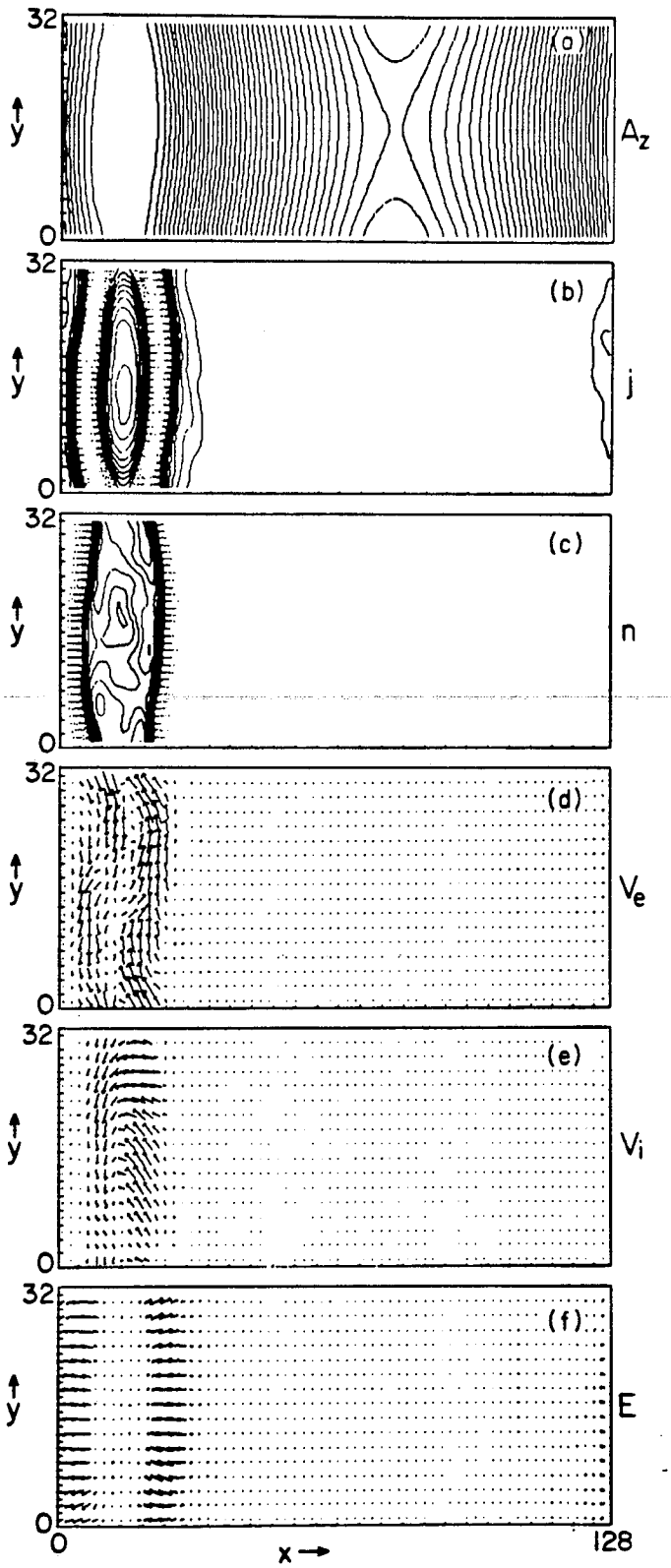

Fig. 6

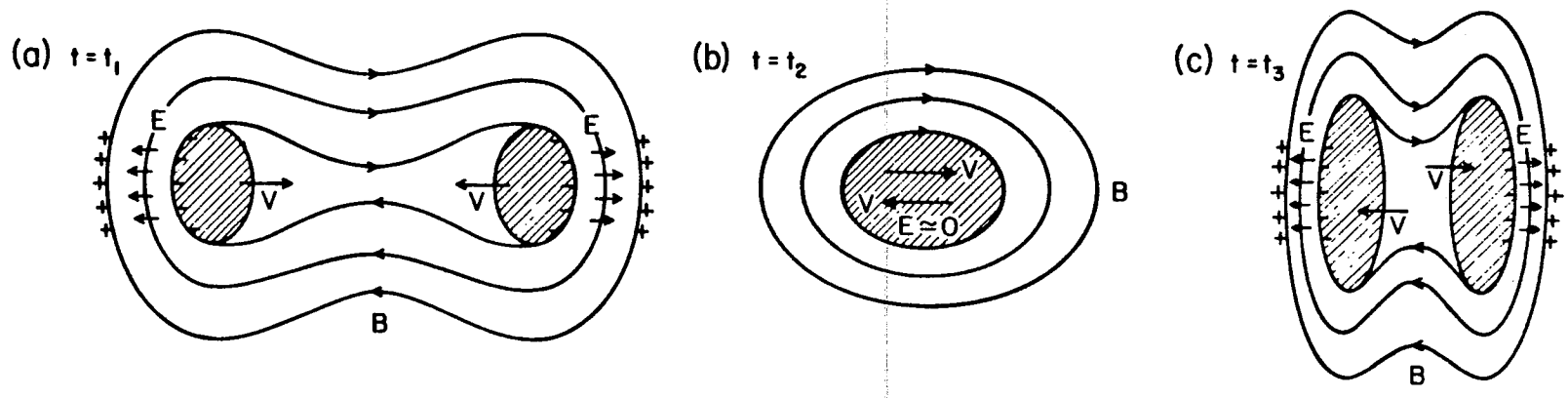

Fig. 7

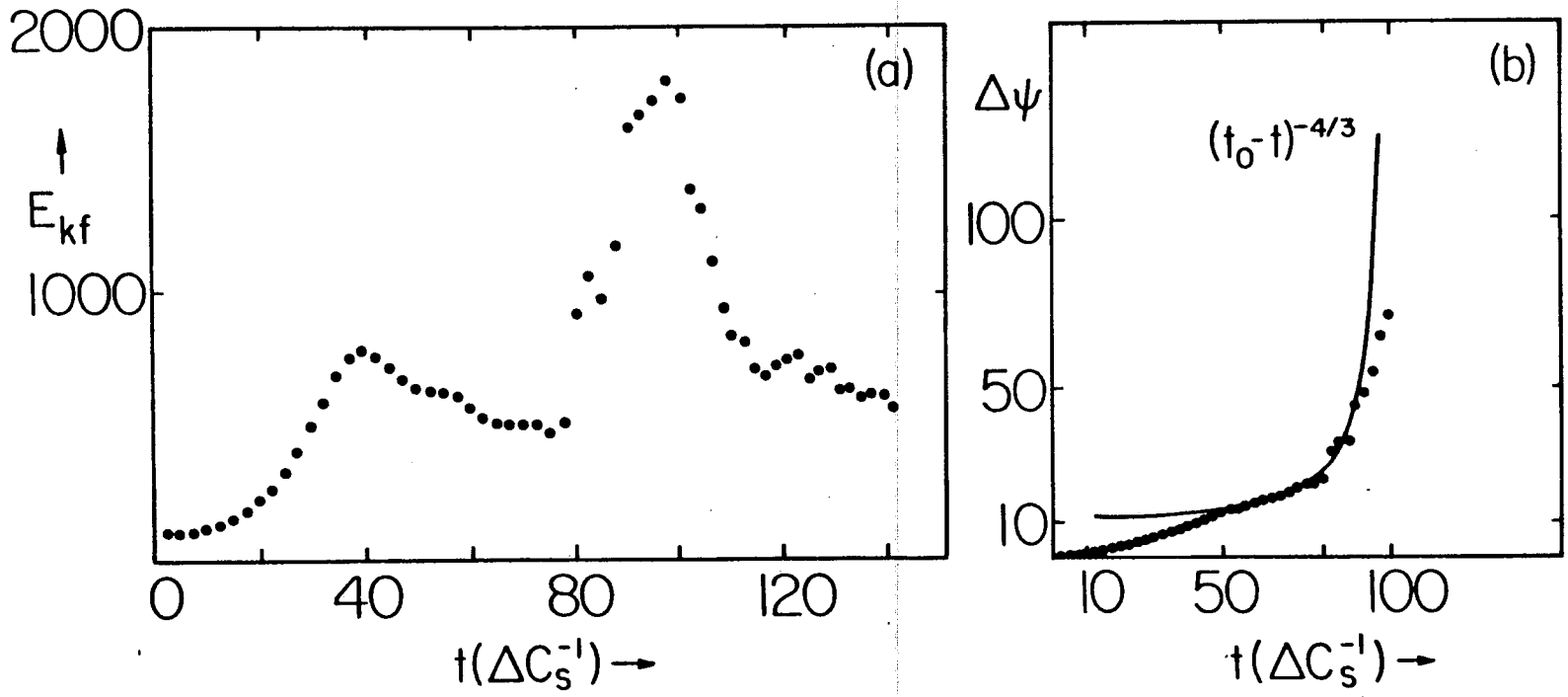
2000
1000
E_{kf}
(a)
0
40
80
120
$t(\Delta C_s^{-1})\rightarrow$
$\Delta\psi$
100
50
10
$(t_0-t)^{-4/3}$
(b)
10
50
100
$t(\Delta C_s^{-1})\rightarrow$

Fig. 8

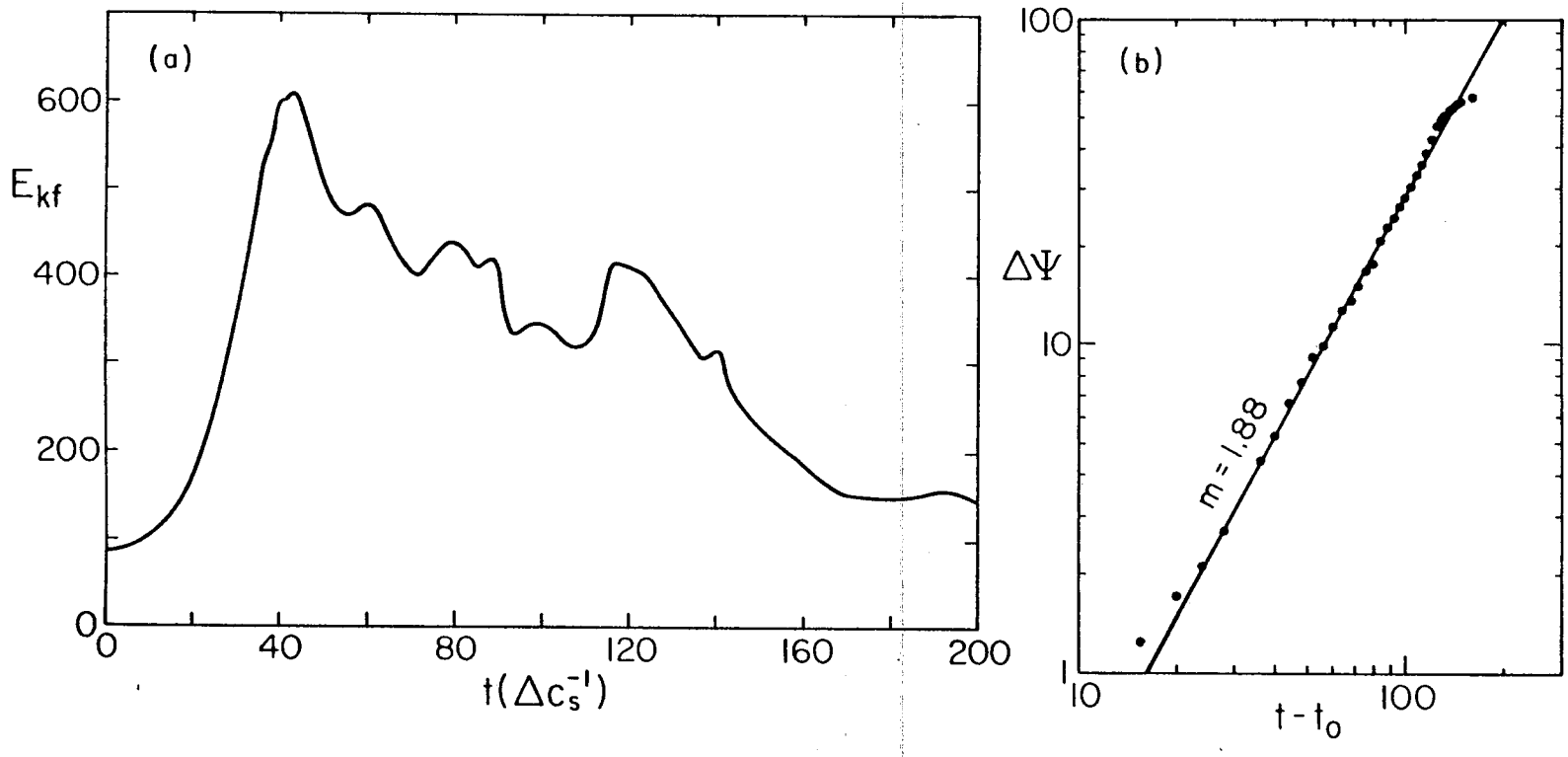
(a)
600
400
200
0
E_{kf}
0
40
80
120
160
200
$t(\Delta c_s^{-1})$
(b)
100
10
1
$\Delta\Psi$
m = 1.88
10
100
$t - t_0$

Fig. 9

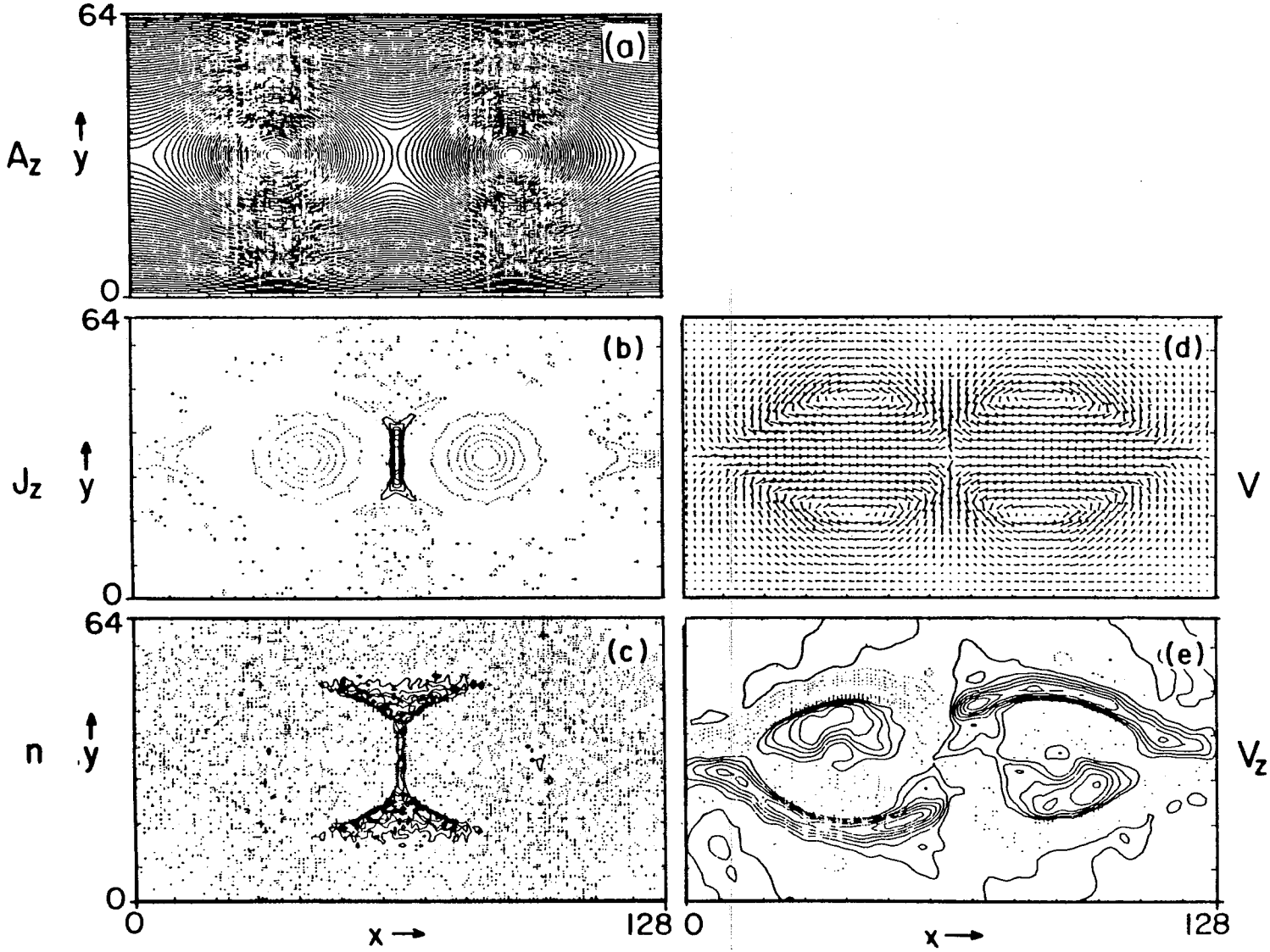

Fig. 10

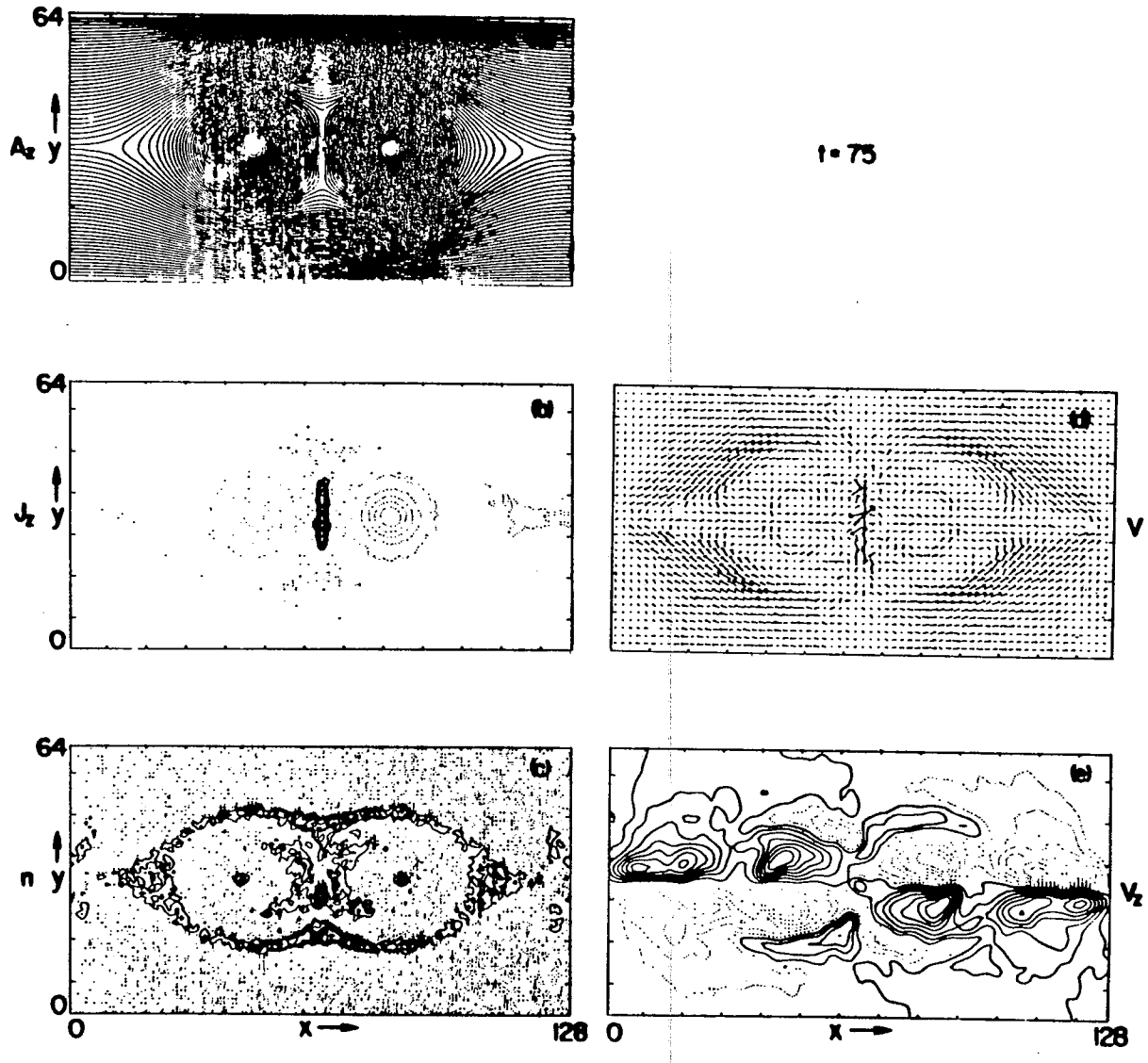

Fig. 11

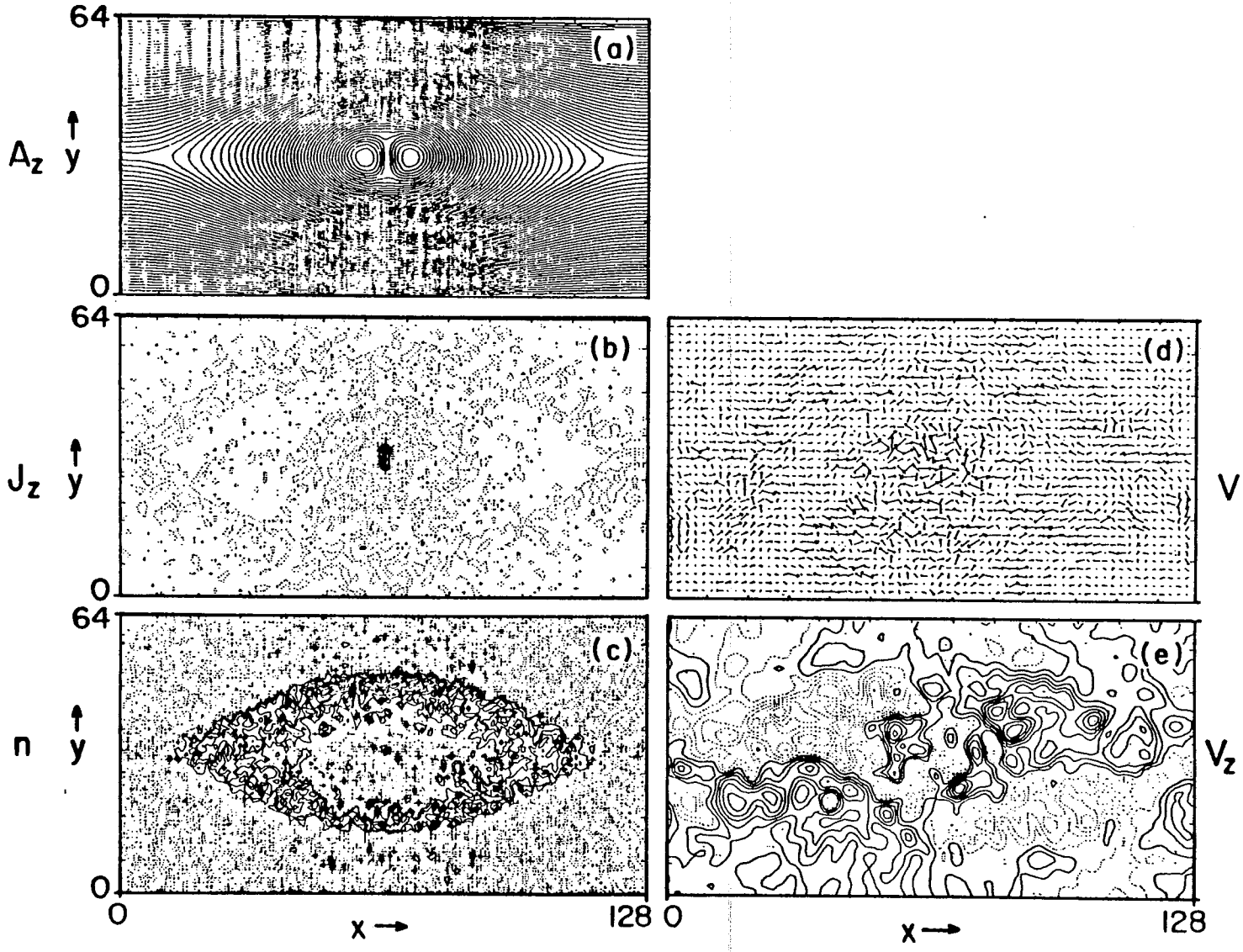

Fig. 12

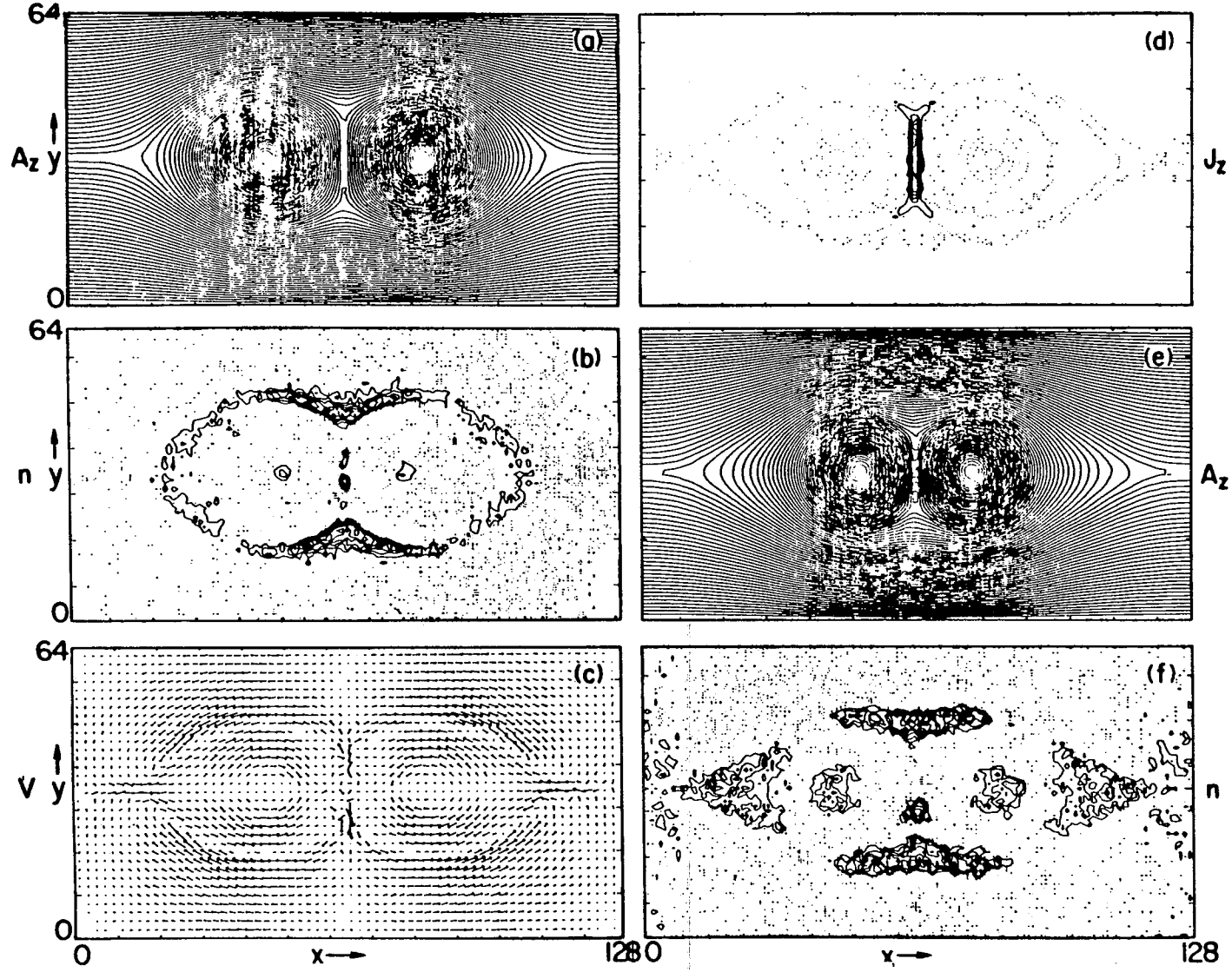

Fig. 13

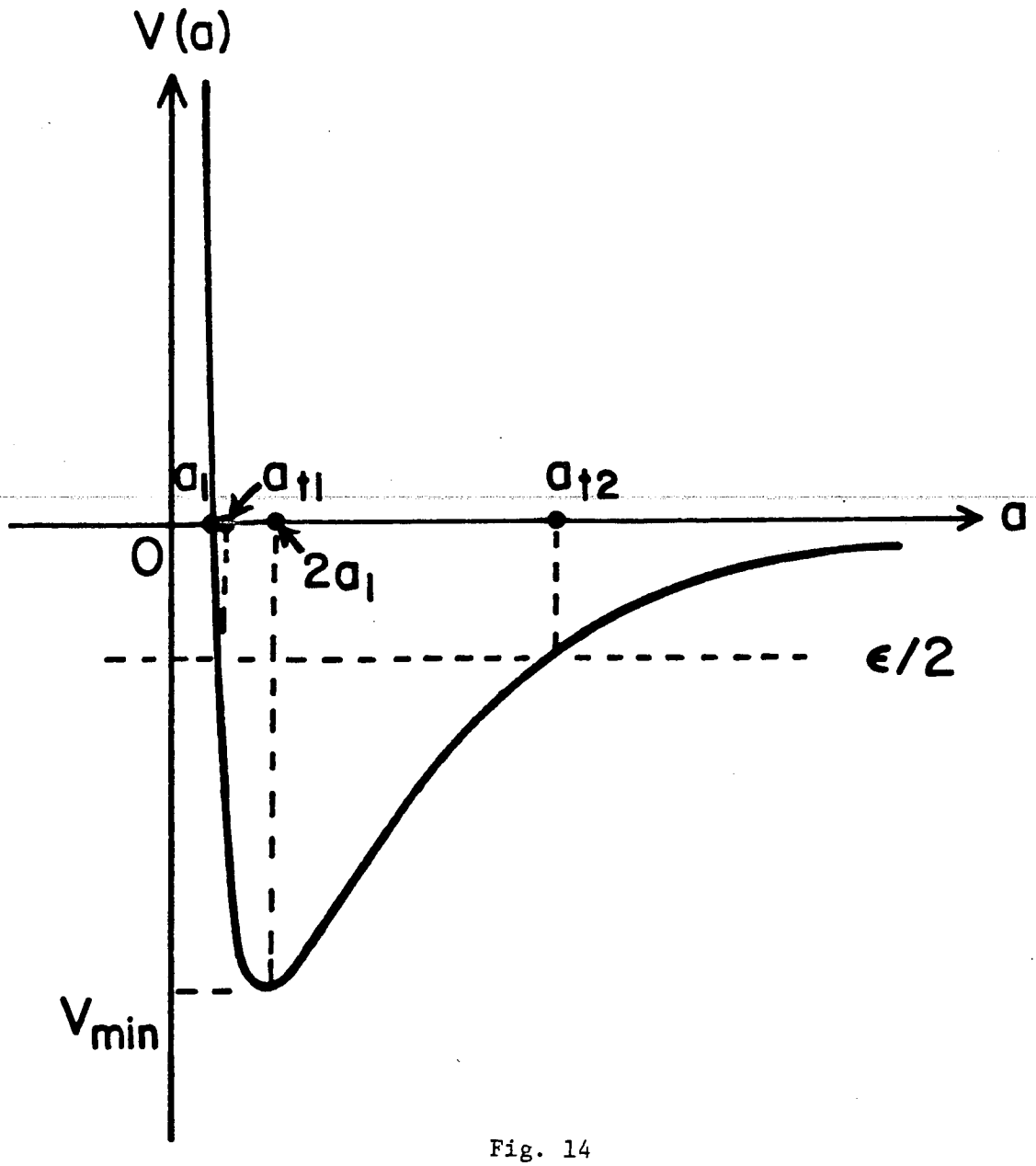

Fig. 14

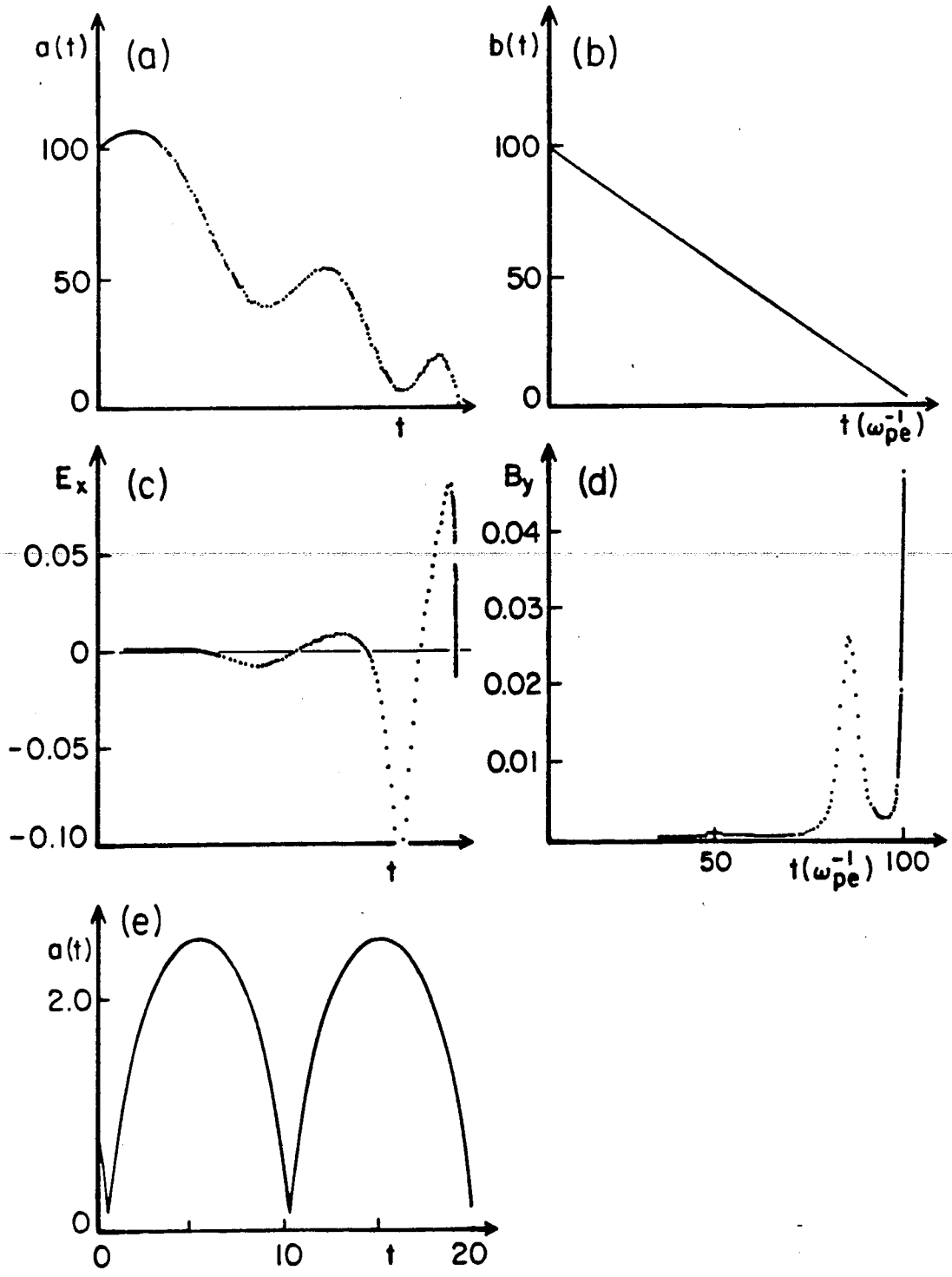
a(t)
(a)
100
50
0
t
b(t)
(b)
100
50
0
t (ω_pe^-1)
E_x
(c)
0.05
0
-0.05
-0.10
t
B_y
(d)
0.04
0.03
0.02
0.01
50
t(ω_pe^-1)
100
(e)
a(t)
2.0
0
0
10
t
20

Fig. 15

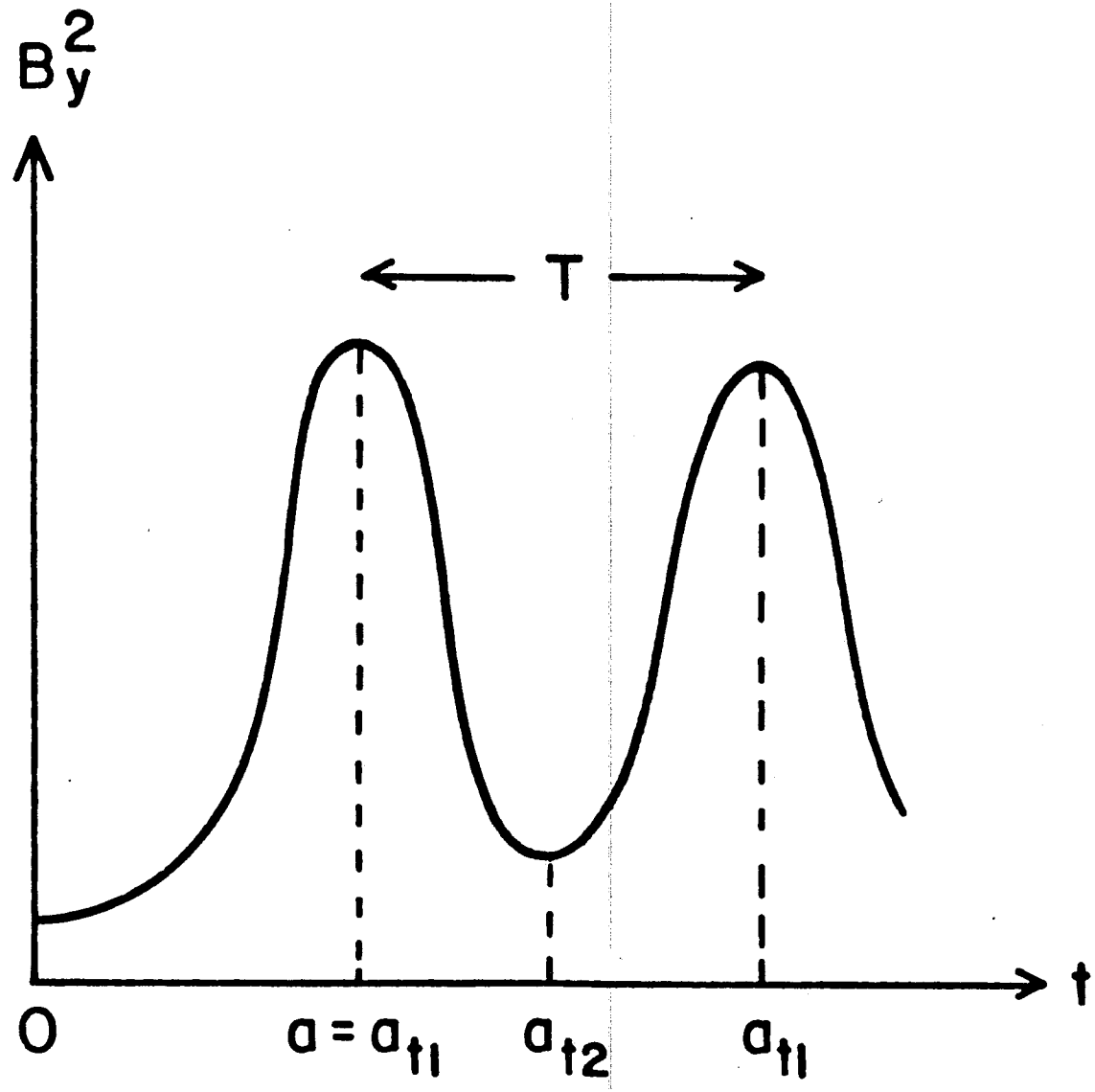

Fig. 16

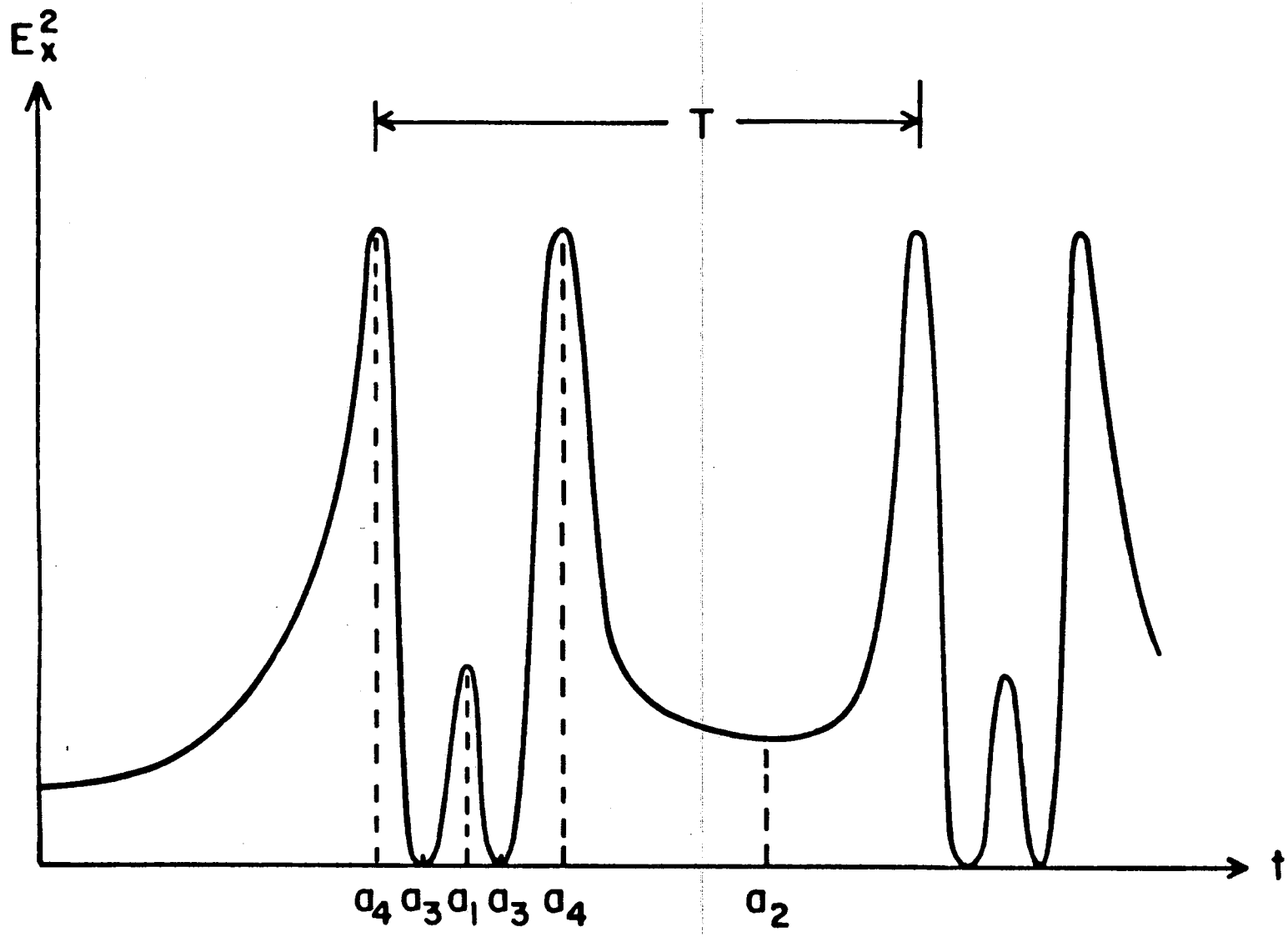

Fig. 17

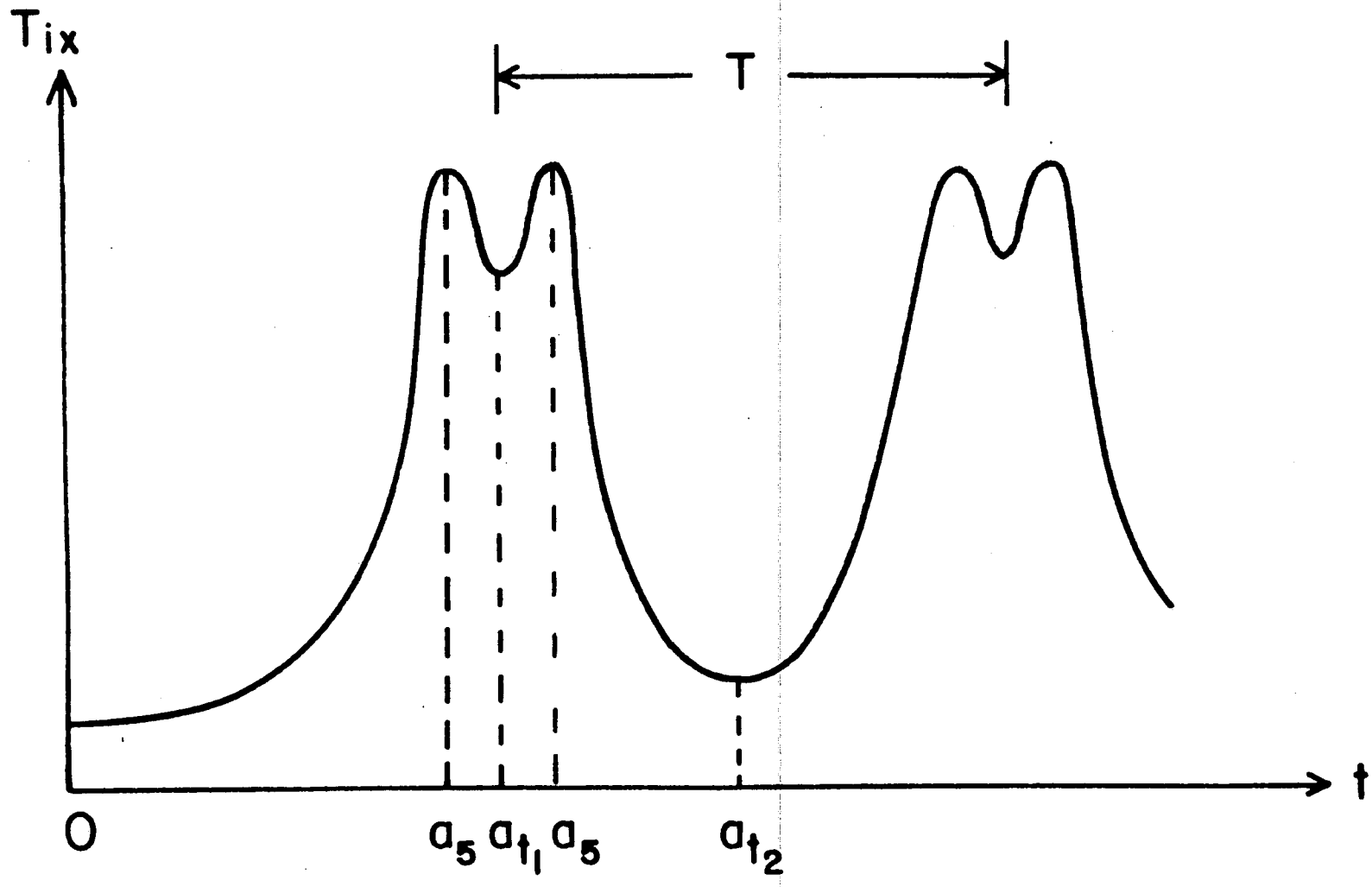

Fig. 18

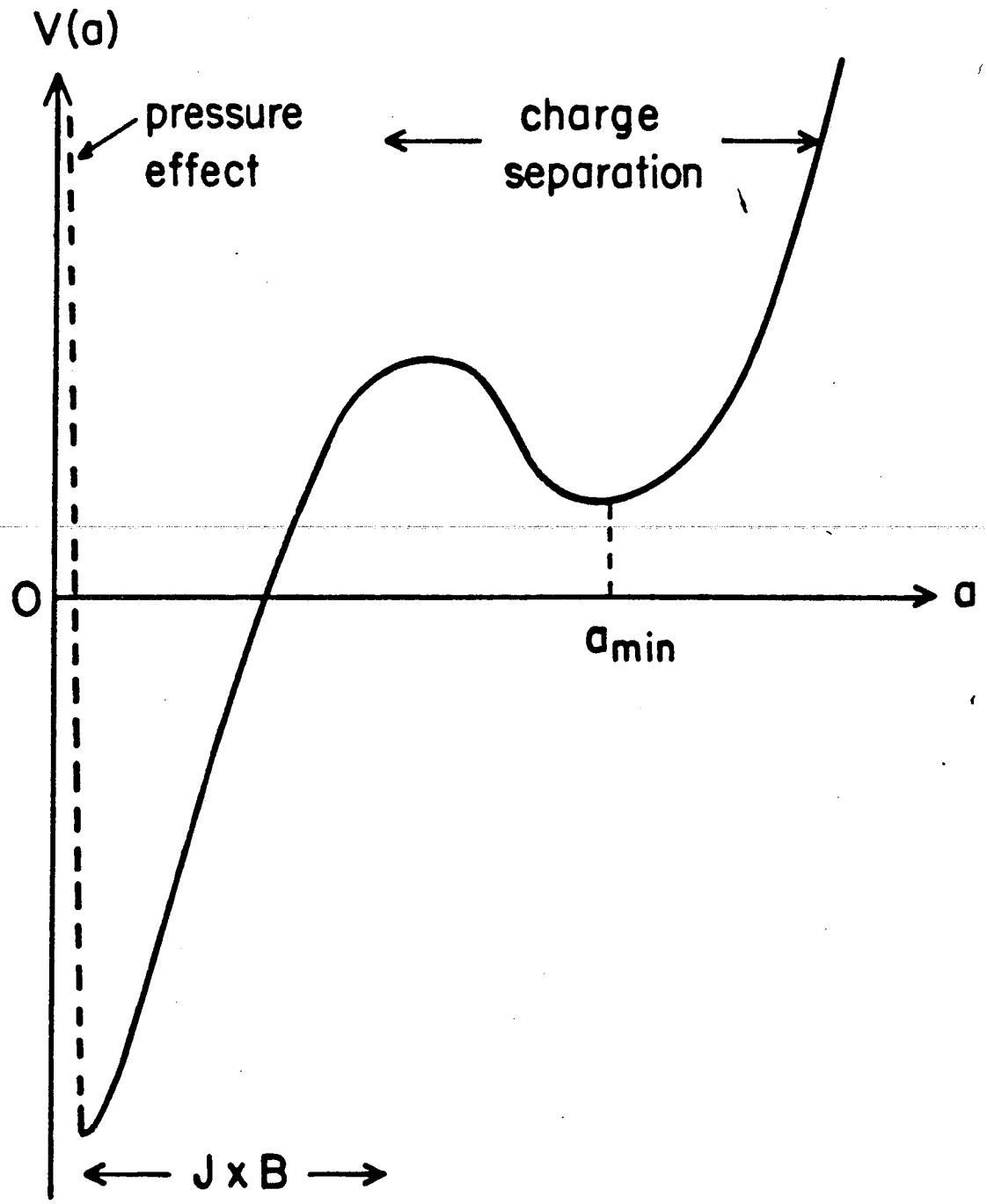

Fig. 19

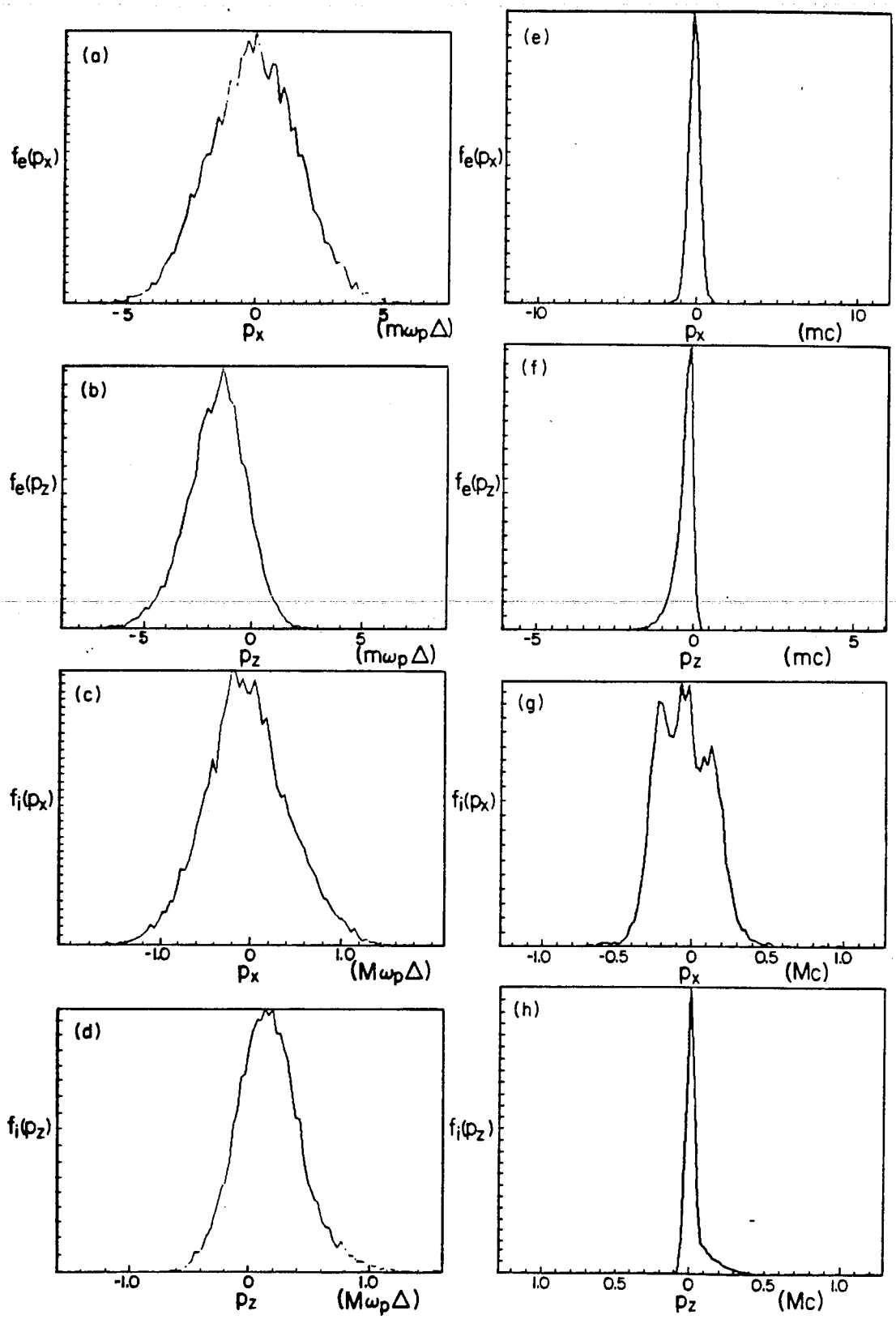
(a)
$f_e(p_x)$
-5
0
5
p_x
$(m\omega_p\Delta)$
(e)
$f_e(p_x)$
-10
0
10
p_x
(mc)
(b)
$f_e(p_z)$
-5
0
5
p_z
$(m\omega_p\Delta)$
(f)
$f_e(p_z)$
-5
0
5
p_z
(mc)
(c)
$f_i(p_x)$
-1.0
0
1.0
p_x
$(M\omega_p\Delta)$
(g)
$f_i(p_x)$
-1.0
-0.5
0
0.5
1.0
p_x
(Mc)
(d)
$f_i(p_z)$
-1.0
0
1.0
p_z
$(M\omega_p\Delta)$
(h)
$f_i(p_z)$
1.0
0.5
0
0.5
1.0
p_z
(Mc)

Fig. 20

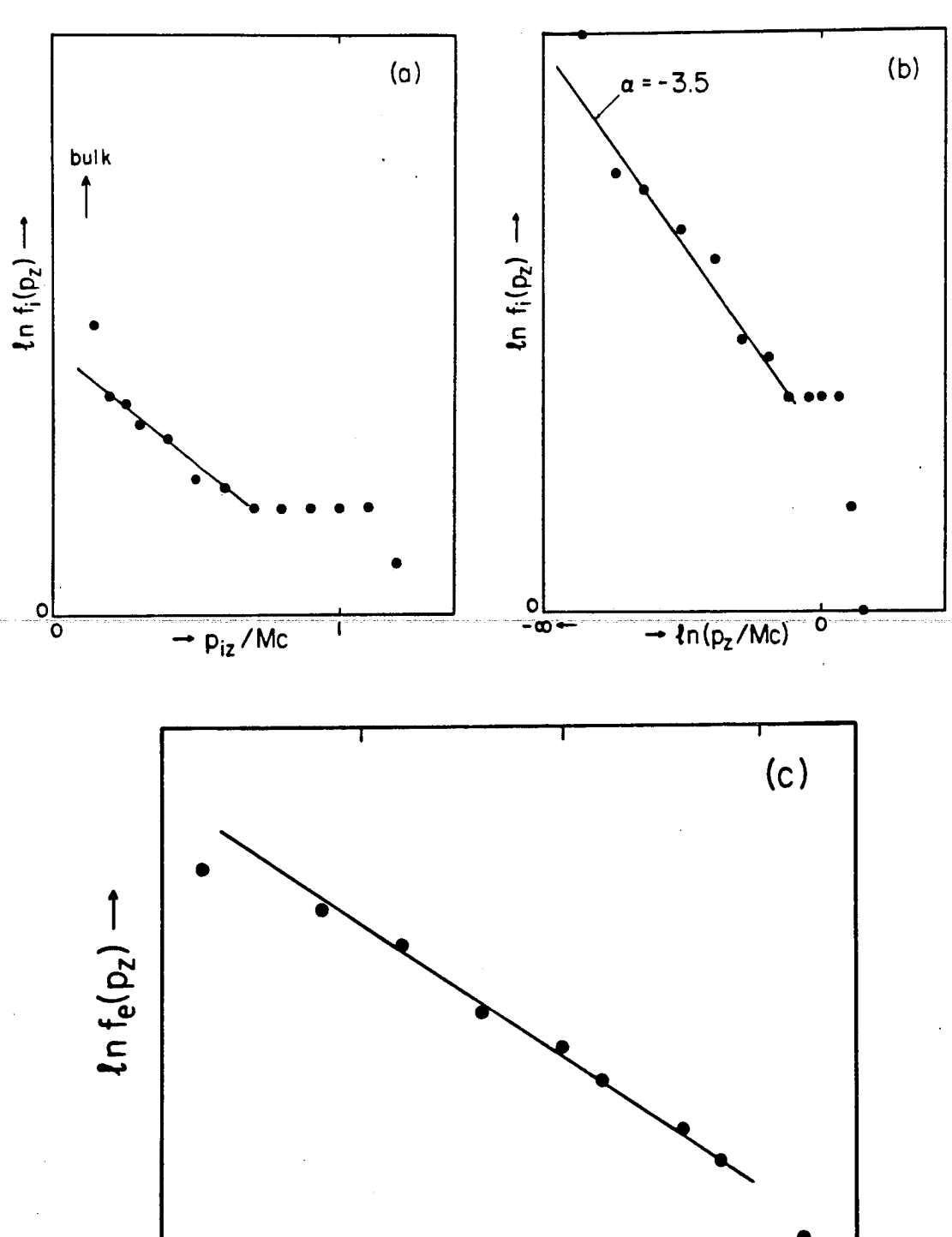
(a)
bulk
ln f_i(p_z)
0
0
1
p_iz / Mc
(b)
α = -3.5
ln f_i(p_z)
0
-∞
ln(p_z/Mc)
0
(c)
ln f_e(p_z)
0
0
1
2
3
p_ez / Mc

Fig. 21

(a)

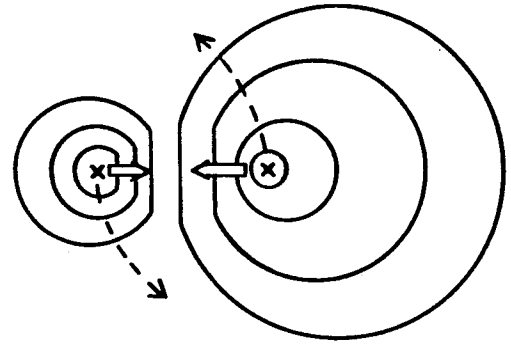

(b)

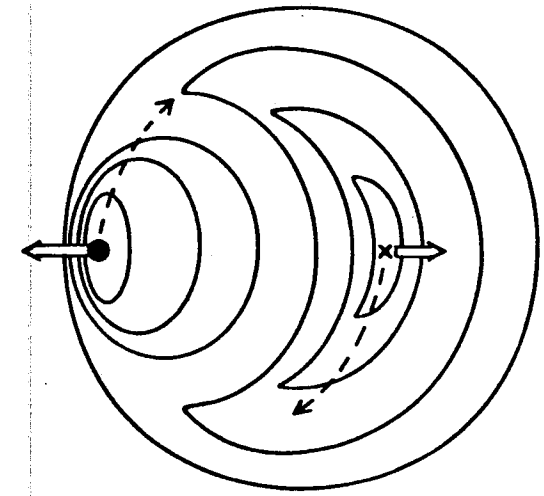

Fig. 22